1　# The role of surface forces in environment-enhanced cracking of brittle solids

2　Mehdi Eskandari-Ghadi[1], Seiji Nakagawa[2], Hang Deng[2], Steve Pride[2], Benjamin Gilbert[2], Yida Zhang[1]

3　**ABSTRACT**

4　　Fracture initiation and propagation in brittle materials is promoted in surface-reactive (sorptive)

5　environments, a phenomenon known as subcritical crack growth (SCG). Laboratory measured crack-

6　propagation velocity vs. stress intensity factor relationships typically exhibit highly nonlinear, multi-

7　stage characteristics that are sensitive to environmental factors such as adsorbate concentration and

8　temperature. For practical purposes, empirical relationships (e.g., a power law) have been used to

9　describe this complex phenomenon. However, how the overall SCG behavior emerges from the

10　underlying fundamental processes near the crack tip, such as the interaction of the crack surfaces

11　separated by only a few nanometers and mass transport within the nano-confined space, is still not well

12　understood. This paper develops a mechanistic, surface-force-based fracture theory (SFFT) which

13　integrates surface force models, fluid transport models, and linear elastic fracture mechanics to

14　quantitatively explain the multi-stage characteristics of SCG in brittle solids. A numerical model is

15　developed based on SFFT and solved through an implicit partitioned scheme for efficiency and

16　modularity. The results are validated by Wiederhorn's data on crack propagation in soda-lime glasses at

17　a wide range of relative humidity levels. We show that, for the first time, the entire range of an SCG

18　curve can be captured by a single physics-based model. The predicted SCG curves reveal that the

19　development of repulsive disjoining pressure behind the crack tip can be responsible for the reduced

20　apparent fracture toughness in a sorptive environment. The shape of the SCG curve, and its changes with

21　respect to the environment, is found to critically depend on the assumed transport models.

22　**Key words**: fracture, kinetics, subcritical crack growth, surface force, sorption.

[1] *Department of Civil, Environmental and Architectural Engineering, University of Colorado Boulder, Boulder, CO*
[2] *Lawrence Berkeley National Laboratory, Berkeley, CA*
* Corresponding author, E-mail address: yida.zhang@colorado.edu

1. BACKGROUND

Subcritical crack growth plays a crucial role in the long-term mechanical performance of natural and engineered materials. In sorptive environments, or as referred to by Rice (1978) the *surface-reactive* environments, stable crack growth with a finite velocity (v_c) can occur at stress intensity factors (K_I) significantly lower than the critical one (K_{IC}) measured under the apparent 'dry' or vacuum conditions. This phenomenon is known as subcritical crack growth (SCG) (Atkinson, 1982) or static fatigue (Charles, 1958). SCG controls the rate of important geological processes such as the diagenesis of granular rocks (Chester et al., 2007) and weathering (Eppes and Keanini, 2017). Because it can be viewed as a precursor to abrupt fracturing, understanding and modeling SCG can help improve the prediction of volcanic eruptions (Kilburn and Voight, 1998) and fault failure (Lennartz-Sassinek et al., 2014). SCG may also contribute to the slow degradation of engineering materials (such as concrete, glass, metal, sand, rock), which is important in civil and mechanical engineering practice (Freiman et al., 2009; Karimpour and Lade, 2010; Le et al., 2009; Simmons et al., 1978; Zhang and Buscarnera, 2018).

The key challenge of quantitative modeling of SCG is rooted in its nonlinear multistage behavior resulted from complex physiochemical interactions at various length scales. SCG typically exhibits three distinct stages in the $v_c - K_I$ space (Fig. 1a). At relatively low K_I (stage I), v_c increases rapidly with K_I due to solid-environment interactions; at intermediate K_I (stage II), v_c is believed to be controlled by the transport of the active species; stage II continues until a sudden and rapid increase of v_c (stage III) as K_I exceeds the intrinsic fracture threshold (K_{IC}) of the material in vacuum (Freiman et al., 2009; Wiederhorn, 1967). The stage I and II curves strongly depend on environmental conditions such as temperature and reactant (adsorbate) concentration in the environment (Fig. 1b) (Crichton et al., 1999; Wiederhorn et al., 1980). In this context, our SCG model aims to address two key questions: (Q1) how

45   do solid and environment interact to cause the reduced fracture toughness (from K_{IC} to K_{I0} in Fig. 1a)

46   and the associated exponential kinetics in stage I? and (Q2) what transport mechanism (or combination

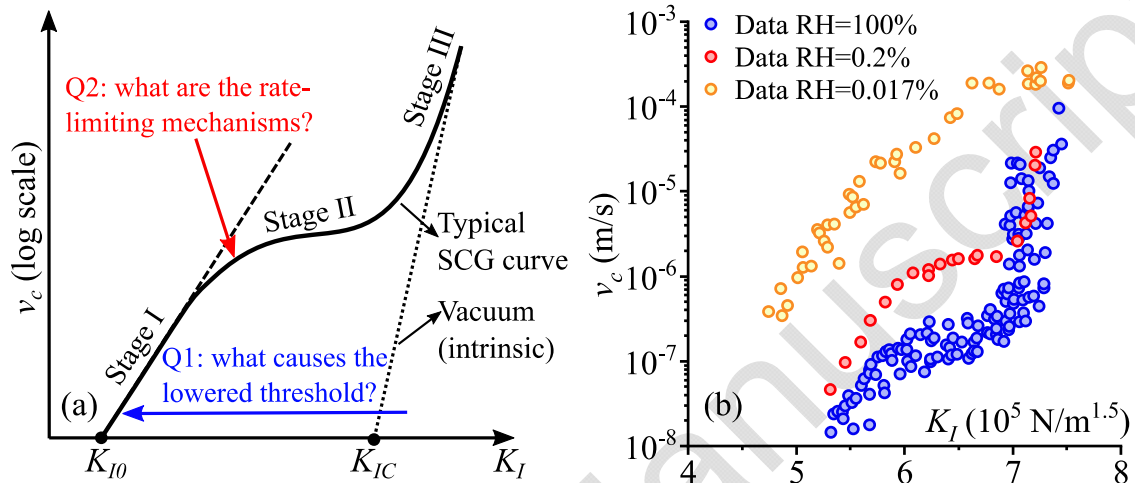47   of mechanisms) is at work near the crack tip to effectively limit the crack velocity in stage II?

48

Fig. 1. (a) Typical SCG curve and the two fundamental questions. (b) SCG data of soda-lime glass at different relative humidity, RH (Wiederhorn, 1967; Wiederhorn et al., 1980).

52   Regarding the first question, many hypotheses have been proposed for different material-

53   environment systems. Energy-based approaches explain the reduction of apparent fracture toughness

54   through the decreased surface energy caused by the adsorption of fluid species on the crack surfaces

55   (Rice, 1978; Wan et al., 1990). In contrast, atomistic approaches focus on crack-tip chemical reactions

56   such as hydrolysis of stretched crack-tip bonds, dissolution and transport of crack tip material, and ion

57   exchange with the crack tip (Atkinson, 1984; Michalske and Freiman, 1982). Concurrent with these

58   mechanisms are the crack kinetic models by making analogy between crack propagation and reaction

59   kinetics (Bazant and Planas, 1997; Lawn, 1975). Alternatively, empirical $v_c - K_I$ relationships such as

60   power law are used as a descriptive tool without considering the underlying mechanisms driving the

61   crack propagation (Bazant and Planas, 1997; Charles, 1958).

62   For the second question, some mechanisms such as Fickian diffusion (Wiederhorn, 1967), Knudsen

63   diffusion (Lawn, 1974), and surface diffusion (Crichton et al., 1999) have been proposed to govern the

64 fluid invasion along a crack. However, the temperature-dependence of SCG data observed in phosphate

65 laser glasses suggests that none of these mechanisms alone can fully describe the stage II behavior

66 (Crichton et al., 1999). Mass transport in nano-confined spaces is still an active area of research (Choi et

67 al., 2001; Cihan et al., 2019) and is poorly understood at this moment for the near-crack-tip region. For

68 these reasons, to this day, the modeling of stage II and the transition from stages I to II remains highly

69 simplistic and phenomenological. Frequently, the stage II and III behaviors are neglected altogether, and

70 only power-law relationships are fitted to the $v_c - K_I$ data obtained in stage I, across a range of stresses

71 and environmental conditions (Brantut et al., 2013; Eppes et al., 2018; Nara et al., 2012; Olson, 1993).

72 Recently, atomic force microscope (AFM) and surface force apparatus (SFA) experiments revealed

73 that repulsive forces (e.g., electrical double layer, hydration, crystallization) can become dominant

74 between mineral surfaces at nanometer separations in the presence of sorptive species (Dziadkowiec et

75 al., 2018; Røyne et al., 2015). Specifically, SFA measurements and molecular dynamic simulations (MD)

76 suggest that the nano-confinement of solutions between calcite surfaces can exert repulsion over

77 hundreds of nanometers of separation (Diao and Espinosa-Marzal, 2016; Dziadkowiec et al., 2019).

78 AFM measurements confirm that forces of similar range exist between glass surfaces in aqueous

79 solutions (Acuña and Toledo, 2008), and their magnitudes depend on the chemical composition of the

80 environmental fluid (Adler et al., 2001). This inspires an alternative explanation of the complex SCG

81 behavior: the repulsive forces along the crack walls can possibly facilitate the initiation and propagation

82 of cracks in sorptive environments, resulting in the characteristic trend of an SCG curve in Fig. 1.

83 Although the potential of surface forces in affecting solid fracture was debated in the glass community a

84 few decades ago (Lawn, 1985; Wiederhorn and Fuller Jr, 1989), it has been largely neglected since then,

85 without much progress.

86

2. A SURFACE-FORCE BASED FRACTURE THEORY

87

88   Provided the renewed evidence of repulsive surface forces induced by surface sorption, we propose

89   an SCG theory to assess a mechanistic, surface-force-based answer to both questions. The key strategy

90   is illustrated in Fig. 2 and explained in the following. In this model, surface forces along crack surfaces

91   are accounted for via a force-separation relation. For a homogenous material in perfect vacuum, $\Pi(w)$

92   is defined by the force required to overcome the solid-solid intermolecular forces in separating two

93   surfaces and is the same everywhere along the crack. The interacting force at different location x along

94   the crack surface can be read from this $\Pi(w)$ curve given the local crack separation $w(x)$. The

95   resistance against crack opening provided by the attractive surface force is macroscopically manifested

96   as the fracture toughness K_{IC} in classical fracture mechanics (Meng and Thouless, 2019). This part is

97   similar to the well-established cohesive crack theory (CCT), where the cohesive forces in the fracture

98   process zone (FPZ) counterbalance the far-field tensile stress to give a net-zero stress intensity factor at

99   the crack tip (Barenblatt, 1962).

100   Now consider that the crack is invaded by sorptive species, resulting in a non-uniform distribution of

101   species concentration $C = C(x)$ along the crack as shown at the bottom of Fig. 2. Intrusion of the

102   sorptive molecules can shift the local $\Pi(w)$ towards the repulsive side (Eskandari-Ghadi and Zhang,

103   2022), the magnitude of which depends on the local chemistry $C(x)$. The surface force at different

104   locations therefore starts to travel along different $\Pi(w)$ curves as opposed to the vacuum case. The

105    $C(x)$ profile is dictated by the species transportation along the crack and is thus coupled with the crack

106   opening profile $w(x)$, the ambient concentration C_0, and the crack velocity v_c. The proposed theory can

107   potentially explain the first question (Q1) through the reduced attraction or the development of repulsion

108   due to the presence of sorptive species. The second question (Q2) can be also directly addressed through

109   the coupling between fracture propagation and species transport in cracks.
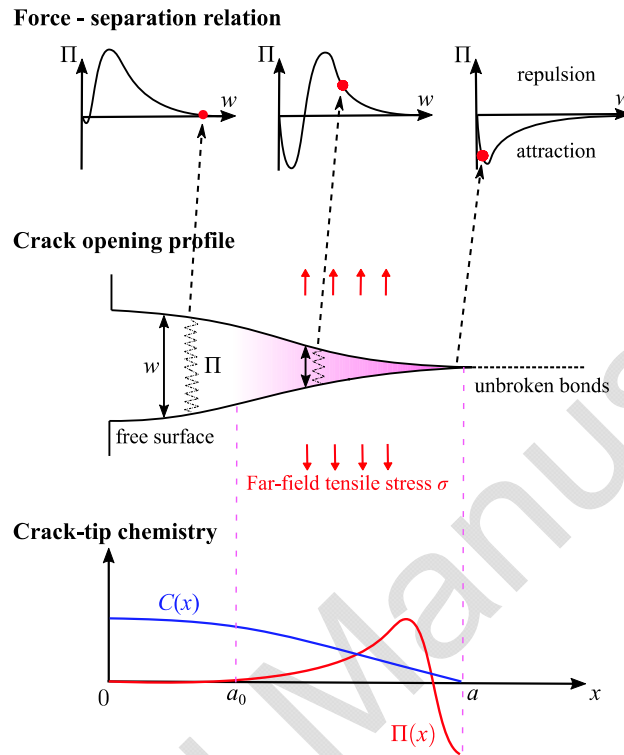

110
111   Fig. 2. The key elements of the proposed surface-force based fracture theory.

112   The proposed theory operates at an intermediate scale which is larger than the atomistic theories

113   without relying on the dynamics of the crack-tip bond but is smaller than the macroscopic energy

114   approaches by requiring the full resolution of crack opening profile and stress fields near the crack tip. It

115   also differs from the cohesive crack theory in that, the traction curve in CCT is a constitutive relation

116   commonly fitted to macroscale fracture testing data, involving only attractive force, and does not vary

117   along the crack. In contrast, the proposed approach is rooted in surface physics, involves intermediate-

118   scale force-separation relationships which are either directly measurable by SFA experiments or

119   theoretically derivable based on intermolecular potentials, and can be strongly repulsive and vary with

120   the local environment. We therefore refer to the proposed theoretical framework as the Surface-Force

121   based Fracture Theory (SFFT) to distinguish from the previous works.

122   The remainder of this paper shall tackle two specific goals: (1) to formalize the mathematical

123   structure of SFFT for mode-I fractures and (2) to numerically implement an SFFT model and test its

124   ability in capturing typical SCG behaviors. For demonstration, the model will be specialized for the

125   glass-in-vapor experiments of Wiederhorn (1967) as our first step towards advancing our general

126   understanding of environment-enhanced cracking of brittle materials. We start by laying out the stress

127   intensity, opening profile, and propagation kinetics of cracks with considering both far-field stress and

128   distributed stresses along the crack surface (Section 3). We then formulate simplified analytical models

129   for surface force under variable environment (Section 4) and species transport along a moving non-

130   parallel slit (i.e., a propagating crack) (Section 5). We numerically solve the system via a partitioned

131   implicit scheme to ensure a robust and efficient coupling between the aforementioned processes (Section

132   6). Finally, the model performance is assessed using the SCG data of soda-lime glass at different

133   humidity levels as presented in Fig. 1b (Section 7). The main conclusions and possible future extensions

134   of this work are discussed at the end (Section 8).

135   **3.   FRACTURE MODELING CONSIDERING SURFACE FORCES**

136   **3.1.   Fracture mechanics analysis**

137   We adopt the approach of Lawn (1985) by directly acknowledging the disjoining pressure (Π) in

138   the LEFM analysis. The *disjoining pressure* Π is here defined as the net surface force between two

139   solid surfaces normalized by the surface area (Clarke et al., 1986). It lumps the contributions of all solid-

140   fluid interactions together without discerning their physiochemical origins and takes a positive value

141   when the net force is repulsive (or disjoining) and negative when cohesive (or joining). Such distributed

142   pressure along the crack surface can alter the stress field, characterized by the *effective* stress intensity

143   factor (K_{Ie}), in the vicinity of the crack tip. K_{Ie} should be distinguished from the applied stress intensity

144   (K_{Ia}) which solely accounts for the external forces or far-field stresses on the cracked solid.

145   Let us consider a 2D (plane-strain) edge crack of finite length a (Fig. 3a) in an elastic half-space

146   subject to far-field tensile stress and disjoining pressure $\Pi(x)$ over the crack surface. The boundary

147   conditions are selected such that the problem is equivalent to an infinite body with a line crack (Irwin,

148   1957) (Fig. 3b). This allows one to take advantage of the readily available fundamental solutions to

149   calculate the mode-I crack opening and stress intensity under various loading combinations (Tada et al.,

150   2000). The dependency of $\Pi(x)$ on fluid chemistry and species transportation will be addressed in
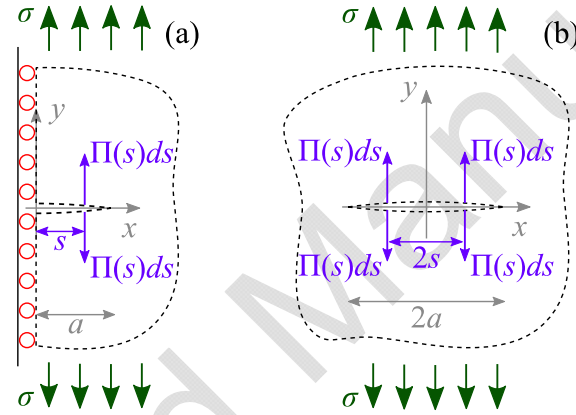
151   section 4.

152
153   Fig. 3. Schematic of the model geometry and loading scenarios. (a) A finite edge crack in semi-infinite elastic domain. (b) A
154   finite center crack in elastic infinite domain. The boundary conditions in (a) guarantee equivalent stress-deformation solution
155   as (b).

156   LEFM allows one to write the effective stress intensity factor in an additive fashion

$$K_{Ie} = \underbrace{k_{I\sigma}\sigma}_{K_{Ia}} + \underbrace{\int_{s=0}^{s=a} k_{I\Pi}(s)\Pi(w(s);s)ds}_{K_{I\Pi}} \tag{1}$$

158   where $k_{I\sigma}$ is the stress intensity factor caused by unit far-field tensile stress; σ is the magnitude of the

159   tensile stress; $k_{I\Pi}(s)$ is the stress intensity factor caused by unit repulsive force on the crack surface at

160   location s ; $w(x)$ is the crack opening at location x ; $\Pi(w)$ describes a disjoining pressure vs.

161   separation relation which will be given by the surface force model (see Section 4); K_{Ia} is the applied

162   stress intensity factor; $K_{I\Pi}$ is the stress intensity contribution by the disjoining pressure and takes a

163   negative value when the net effect of Π is cohesive.

164   For a given σ, the distribution $\Pi(x) = \Pi(w(x); x)$ is not known a priori. Π depends on the surface

165   separation while its change in turn alters the crack opening profile. The expression of $w(x)$ is given

166   below based on LEFM (Bazant and Planas, 1997):

167
$$w(x) = c_\sigma(x)\sigma + \int_{s=0}^{s=a} c_\Pi(x,s)\Pi(w(s);s)ds \tag{2}$$

168   where $c_\sigma(x)$ is the crack opening at location x along the crack caused by unit far-field tensile stress;

169    $c_\Pi(x,s)$ is the crack opening at the same location caused by a unit repulsive force at location s.

170   For the geometry sketched in Fig. 3a and b, $k_{I\sigma}$ and $c_\sigma(x)$ are given by Tada et al. (2000)

171
$$k_{I\sigma} = \sqrt{\pi a} \text{ and } c_\sigma(x) = \frac{4(1-v^2)}{E}\sqrt{a^2 - x^2} \tag{3}$$

172   Similar fundamental solutions can be found for unit surface force applied at s:

173
$$c_\Pi(x,s) = \frac{8(1-v^2)}{\pi E}\begin{cases} \tanh^{-1}\sqrt{\dfrac{a^2 - s^2}{a^2 - x^2}} & ; & x < s \\[4mm] \coth^{-1}\sqrt{\dfrac{a^2 - s^2}{a^2 - x^2}} & ; & x > s \end{cases} \tag{4}$$

174
$$k_{I\Pi}(s) = 2\sqrt{\frac{a}{\pi}}\frac{1}{\sqrt{a^2 - s^2}} \tag{5}$$

175   It should be noted that Eqns. (4) and (5) are singular at $x = s$. This introduces difficulties to the

176   numerical integrations of Eqns. (1) and (2). We have circumvented this difficulty by means of numerical

177   approximation which allows the usage of non-singular analytical solutions (see Appendix A for details).

178   The non-linear coupling between $w(x)$ and $\Pi(w)$ can be assembled as a system of two algebraic

179   equations, referred to as the $\Pi - w$ system hereafter, to be solved simultaneously (see Appendix A). The

180   solution to the $\Pi - w$ system provides a crack opening profile $w(x)$ which will be substituted into Eq.

181   (1) in conjunction with the $\Pi(w)$ model (see Section 4) to obtain K_{Ie}.

3.2. Crack propagation kinetics

183   The rate at which crack propagates can be studied in the framework of reaction rate theory (Charles,

184   1962). Griffith's criterion suggests that non-dissipative crack propagation occurs once $(\mathcal{G} - 2\gamma) > 0$,

185   where $\mathcal{G}$ is known as the energy release rate and γ is the surface tension of the newly created crack

186   faces. By analyzing the statistics of bond breakage and healing under the energy difference $(\mathcal{G} - 2\gamma)$ in a

187   way similar to a chemical reaction driven by chemical potential differences (Lawn, 1975), one can arrive

188   at the following kinetic equation

$$189 \qquad v_c = v_0 \exp\left(-\frac{Q_0}{RT}\right)\sinh\left(\frac{\tilde{\kappa}_0(\mathcal{G} - 2\gamma)}{RT}\right) \qquad (6)$$

190   where $\tilde{\kappa}_0$ is a proportionality factor; Q_0 is the activation energy for bond breaking; v_0 contains

191   information of the solid lattice vibration frequency and lattice length-scale (Meng and Thouless, 2019).

192   In Eq. (6), the "driving force" for crack propagation is $(\mathcal{G} - 2\gamma)$. Bazant and Planas (1997) have shown

193   that stress intensity factor can be also taken as the driving force to replace $(\mathcal{G} - 2\gamma)$ in Eq. (6). Inspired

194   by this, we propose a slightly different equation for crack growth in the presence of disjoining pressure

$$195 \qquad v_c = v_0 \exp\left(-\frac{Q_0}{RT}\right)\sinh\left(\frac{\kappa_0 K_{Ie}}{RT}\right) \qquad (7)$$

196   where κ_0 is a proportionality factor related to $\tilde{\kappa}_0$. The decomposition of K_{Ie} to K_{Ia} and $K_{I\Pi}$ (i.e., Eq.

197   (1)) reveals some connections between Eqns. (6) and (7). Firstly, the celebrated Irwin equation directly

198   links K_{Ia} and $K_{I\Pi}$, respectively, to $\mathcal{G}$ and 2γ at equilibrium. $K_{Ie} = 0$ implies that $\mathcal{G} = 2\gamma$ and $v_c = 0$,

199   agreeing that a non-propagating crack attains zero stress intensity and thus finite tensile stress at the tip

200   (Barenblatt, 1962). Secondly, the generation of repulsive disjoining pressure in sorptive environment

201   will reduce $K_{I\Pi}$ (Eq. (1)), thus promoting crack propagation under the same applied K_{Ia}. This is

202   equivalent to the surface energy reduction mechanism discussed by Rice (1978). We further argue that

203   Eq. (7) has the unique advantage of directly incorporating the nonuniform reduction of surface energy

204   along the crack (via $K_{I\Pi}$) caused by transient processes such as fluid transport, the inclusion of which in

205   energy-based descriptions is not straightforward.

206   **4. SURFACE FORCE MODEL**

207   The magnitudes of surface forces depend on the crack aperture w (Bazant and Planas, 1997) as well

208   as the local environment C (Israelachvili, 2011). The net effect of these forces over unit surface area

209   can be collectively encapsulated in the disjoining pressure $\Pi(w,C)$, the modeling of which is essential

210   for the proposed fracture theory. Before tackling this task, we should clarify the ambiguity related to the

211   definition of "crack tip".

212   From an atomistic perspective, the crack tip may be defined at the location where the solid chemical

213   bonds are broken. Thermodynamically, one may define the crack tip as the point behind which the

214   separation of opposite surfaces is irreversible and involves energy dissipation, and in front of which the

215   separation occurs reversibly or elastically. Indeed, the location of the "crack tip" behind and ahead of

216   which different inelastic processes may be at work is only a matter of perspective and convenience (Sills

217   and Thouless, 2015). From a continuum point of view, undamaged material obeys elastic behavior, and

218   the damaged material in the fracture process zone (FPZ) obeys a softening stress-strain relation (Bažant

219   and Oh, 1983). The point of divergence between continuum and localized crack happens at the

220   maximum value of traction on the force-separation curve. This motivates us to define the crack tip as the

221   point of maximum traction between two surfaces, and the corresponding crack separation at this

222   reference point is taken as $w = 0$ (See Fig. 4).

223   The consideration of purely cohesive interactions (traction) over several micrometers behind crack

224   tip leads to the well-known cohesive crack theory. It has been successfully applied, for example, to

225   remove the stress singularity predicted by LEFM at the crack tip (Barenblatt, 1962), model the kinetics

226   of crack growth (Meng and Thouless, 2019), and capture crack fatigue (Allegri, 2020; Nguyen et al.,

227   2001). It also hosts various material-specific fracture models by treating the traction-separation curve as

228   a constitutive relation (Hillerborg et al., 1976; MAI and Lawn, 1987; Needleman, 1990; Tijssens et al.,

229   2000; Tvergaard and Hutchinson, 1992). However, the true surface forces originated from the physical

230   separation (<100 nm) of solid surfaces (electrostatic, van der Waals, etc.) and environmental attack

231   (surface hydration, electrical double layer, etc.) has been mostly neglected in classical fracture analysis.

232   The goal here is to substantialize a $\Pi(w, C)$ model to capture these nanometer-scale interactions which

233   can be attractive or repulsive.

234   Generally, the disjoining pressure between two solid surfaces in arbitrary environment can be

235   decomposed into two contributions:

236
$$\Pi(w, C) = \Pi_0(w) + \Delta\Pi(w, C) \tag{8}$$

237   where C stands for the concentration of the sorptive species in between surfaces. C could be

238   generalized to a vector $\mathbf{C} = [C_1, C_2, \ldots, C_k]$ should multiple sorptive species present in the environment.

239   The first component, Π_0, accounts for the intrinsic surface forces between two solid surfaces in vacuum;

240   the second term, $\Delta\Pi$, collects the change of disjoining pressure due to solid-species interaction (Adapa

241   and Malani, 2021; Dziadkowiec et al., 2018; Røyne et al., 2015).

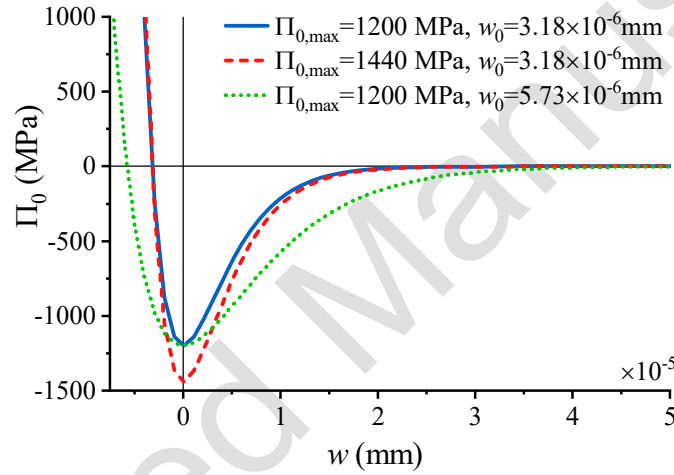### 4.1. Surface force in vacuum $\Pi_0(w)$

$\Pi_0(w)$ may be constructed through smooth interpolations of experimental data provided by SFA/AFM measurements, or rigorously derived with the knowledge of the total intermolecular pair potentials of the solid (Israelachvili, 2011). Here we opt for a well-behaved and versatile analytical expression to represent the in-vacuum surface forces of generic materials. Simple analytical models also benefit the numerical implementation in terms of both convergence and efficiency. A two-parameter equation is adopted for this purpose:

$$\Pi_0 = -\Pi_{0,\max} \frac{w + w_0}{w_0} \exp\left(1 - \frac{w + w_0}{w_0}\right) \tag{9}$$

where Π_0 attains maximum attraction $\Pi_{0,\max}$ at $w = 0$ and decays exponentially for $w > 0$, the rate of which is controlled by w_0. Eq. (9) also contains an exponentially increasing repulsive branch for $w < 0$, which physically corresponds to the steric repulsion when molecules are brought too close together (Israelachvili, 2011). This feature is also expected to be numerically beneficial by serving as a penalty contact to avoid the overlap of two surfaces when they come to contact, in cases where crack healing may occur (i.e., $K_{Ie} < 0$). Eq. (9) is visualized in Fig. 4 for three sets of parameters.

The solution of Eqns. (2) and (9) together allows us to study crack opening at different levels of applied far-field stress in vacuum. Using the numerical method detailed later in Section 6 and parameters in Table 1, the w and Π_0 profiles for a crack of length 36mm under increasing stresses are plotted in Fig. 5. When the stress is low, the in-vacuum surface force contribution of stress intensity $K_{I\Pi}$ can effectively balance out the applied stress intensity K_{Ia}, thus gives a low K_{Ie} value and a near-equilibrium crack per Eq. (7). This results in a smoothly converging crack tip profile (the solid blue curve in Fig. 5a). This is consistent with Barenblatt (1962) who analytically showed that the crack

263   opening profile in the immediate vicinity of the crack tip becomes proportional to the 1.5 power of the

264   distance from the crack tip when $K_{Ie} \to 0$ (the dashed cyan curve). As the applied force increases, the

265   crack is perturbed further away from equilibrium, and its tip geometry becomes blunt and approaches an

266   elliptical shape. Besides the near-tip region, the overall crack opening profile (Fig. 5b) does not vary

267   significantly for the range of applied σ, except for a proportional widening of the crack with increasing

268   σ. Fig. 5c shows that the resultant Π_0 increasingly concentrates at the crack tip as the applied stress

269   increases and the crack aperture widens up.

270
271   Fig. 4. The in-vacuum surface force described by Eq. (9). $\Pi_{0,max}$ controls the magnitude of Π_0 while w_0 controls its spread
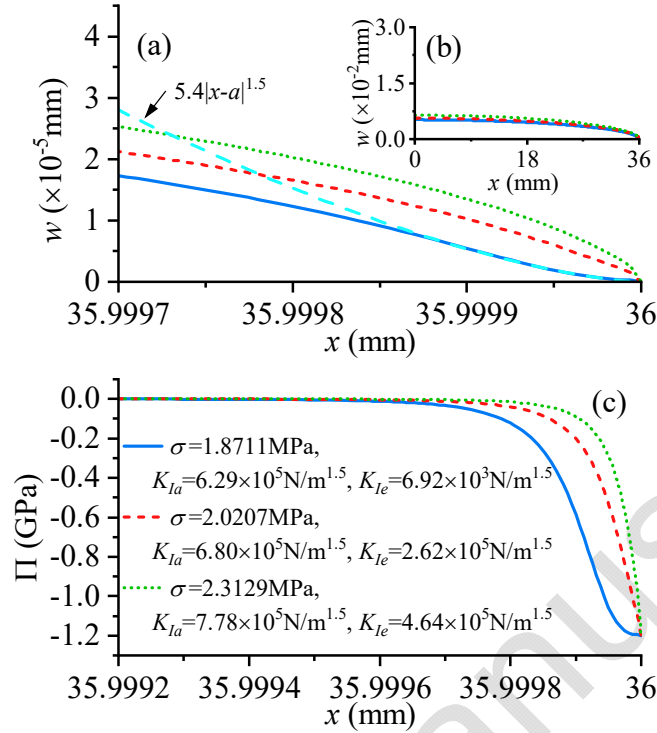272   along w.

Fig. 5. The computed (a) crack tip opening profile, (b) overall crack opening profile, and (c) disjoining pressure distribution in vacuum for progressively increasing far-field tensile stress. The model parameters used here are listed in Table 1.

Figures 6a and 6b plot the computed K_{Ie} and $K_{I\Pi}$ against a wide range of applied K_{Ia} using the same parameters as Fig. 5. As expected, the presence of cohesive forces results in a reduced K_{Ie} compared to K_{Ia}. Increasing K_{Ia} results in a decrease of $K_{I\Pi}$ (Fig. 6b), and thus K_{Ie} asymptotes towards K_{Ia} (Fig. 6a). Lawn (1985) analytically derived an expression of $K_{I\Pi}$ as $K_{I\Pi} = -E'\gamma / K_{Ie}$, where $E' = E/(1-\nu^2)$ for plane-strain, by neglecting the dependence of crack opening profile on Π_0. For the selected parameters, this approximation is surprisingly accurate for large K_{Ia} values but deviates from our exact solution of the full $\Pi - w$ system at lower K_{Ia} levels (Fig. 6b). This implies that the consideration of the two-way coupling between Π and w is essential for studying the onset of SCG which always occurs at low K_{Ia} values. Fig. 6c shows that $K_{I\Pi}^2 / E'$ asymptotes to 2γ as equilibrium ($K_{Ie} = 0$) is approached. This further supports our arguments that Eq. (7) can be viewed as the

286 mechanistic counterpart to Eq. (6), and the Irwin's equation respectively links K_{Ia} and $K_{I\Pi}$ to $\mathcal{G}$ and

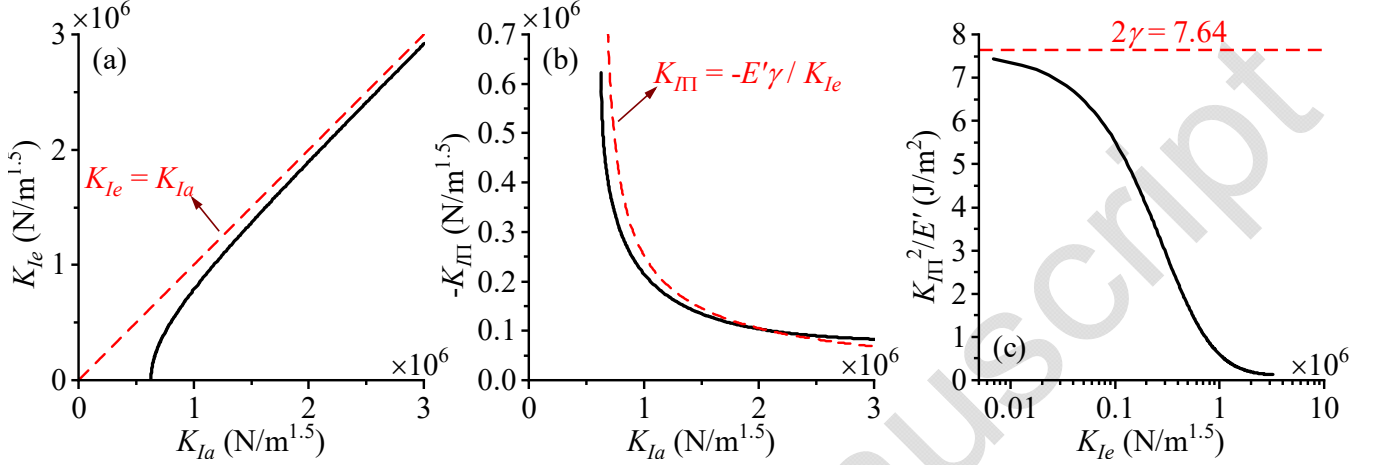287 2γ at equilibrium.

288
289 Fig. 6. Solutions of the $\Pi - w$ system in terms of (a) K_{Ie} versus K_{Ia} to compare with the prediction by Lawn (1985); (b)
290 $-K_{I\Pi}$ versus K_{Ia} to compare with the approximate analysis by Lawn (1985); and $K_{I\Pi}^2 / E'$ versus K_{Ie} to study the
291 application of Irwin's equation in linking $K_{I\Pi}^2 / E'$ and 2γ at equilibrium. E' is the elastic constant and equal to $E/(1-v^2)$
292 for plane strain condition. Parameters used are summarized in Table 1,

4.2. Induced disjoining pressure $\Delta\Pi$

294   The magnitude of $\Delta\Pi$ depends on both the surface separation w as well as the local concentration

295 of sorptive species C (Adler et al., 2001; Eskandari-Ghadi and Zhang, 2021). To construct a $\Delta\Pi$ model,

296 let us focus the discussion on Wiederhorn (1967)'s glass-in-vapor system from hereon. Particularly, we

297 consider a single mode-I crack propagation in soda-lime glass in gaseous nitrogen at 25° with variable

298 relative humidity. The relevant chemistry along the crack can be straightforwardly characterized by the

299 partial pressure of the water vapor p. In this setting, the environment-induced disjoining pressure can

300 be expressed by $\Delta\Pi(w, p)$. Note that we did not consider $\Delta\Pi$ as a function of time in this first

301 treatment. In other words, we have assumed that the adsorption kinetics is much faster than the rate of

302 subcritical crack propagation ($< 10^{-4}$ m/s), and the only rate-limiting step in generating the repulsive

303 disjoining pressure $\Delta\Pi$ is the transport of water vapor along the crack, as described by the transport

304 models detailed in the next section.

305   Physically, many molecular-scale mechanisms can lead to the generation of $\Delta\Pi$ at various vapor

306 pressures (Clarke et al., 1986). It is believed that these mechanisms mainly have origins in Van der

307 Waals, electric double layer, and hydration forces, with the hydration force being the dominant

308 contribution (Dziadkowiec, 2019). The exhaustive discussion of each of them is beyond the scope of this

309 work. A smooth 4-parameter model is instead adopted for the environment-induced disjoining pressure:

310 $$\Delta\Pi(w, p) = f_{\Delta\Pi}(w)g_{\Delta\Pi}(p) \tag{10}$$

311 where

312 $$f_{\Delta\Pi}(w) = \begin{cases} \Delta\Pi_{max} \dfrac{w + \tilde{w}_0}{\tilde{w}_0} \exp\left(1 - \dfrac{w + \tilde{w}_0}{\tilde{w}_0}\right) & ; \ w \geq 0 \\ f_{\Delta\Pi}(0) & ; \ w < 0 \end{cases} \tag{11}$$

313 captures the dependency of $\Delta\Pi$ on w by taking similar form as Eq. (9); and

314 $$g_{\Delta\Pi}(p) = \left(\dfrac{p}{p_{sat}}\right)^{\alpha} \exp\left(\beta\left(1 - \dfrac{p_{sat}}{p}\right)\right) \tag{12}$$

315 characterizes the dependency of $\Delta\Pi$ on the vapor pressure p. $\Delta\Pi_{max}$, $\tilde{w}_0$, α, and β are model

316 parameters; p_{sat} is the saturation vapor pressure. The $f_{\Delta\Pi}$ expression exhibits an overall exponential

317 decay, which is consistent with expressions adopted for hydration forces (Dziadkowiec et al., 2018;

318 Israelachvili, 2011). The expression of g is constructed to 1) monotonically increase with increasing

319 water vapor pressure p, 2) smoothly increase from zero, and 3) contain parameters that control the

320 pressure and the steepness of the steepest increase. The value of $f_{\Delta\Pi}$ in the range of $w < 0$ is assigned to

321 ensure the overall Π model is smooth at w=0. Eqns. (10), (11), (12) and the total Π from Eq. (8) are

322 visualized in Fig. 7 for different levels of p / p_{sat} and values of model parameters. Fig. 7a shows that

323 parameters $\Delta\Pi_{max}$ and $\tilde{w}_0$, respectively and independently, control the spread of $\Delta\Pi$ over separation

324   and its magnitude. Fig. 7b shows that the overall curvature of $g_{\Delta\Pi}$ decreases with increasing α and β.

325   α also controls the curvature at very small p values, while the effect of β is less concerned with small

326   p. The resultant $\Delta\Pi$ in Fig. 7c resembles the disjoining pressure sketched in Ash et al. (1973) and the

327   one derived by Eskandari-Ghadi and Zhang (2021) based on the BDDT isotherm (Brunauer et al., 1940).

328   The total Π in Fig. 7d can be compared with the conceptual sketch by Røyne et al. (2015) for calcite
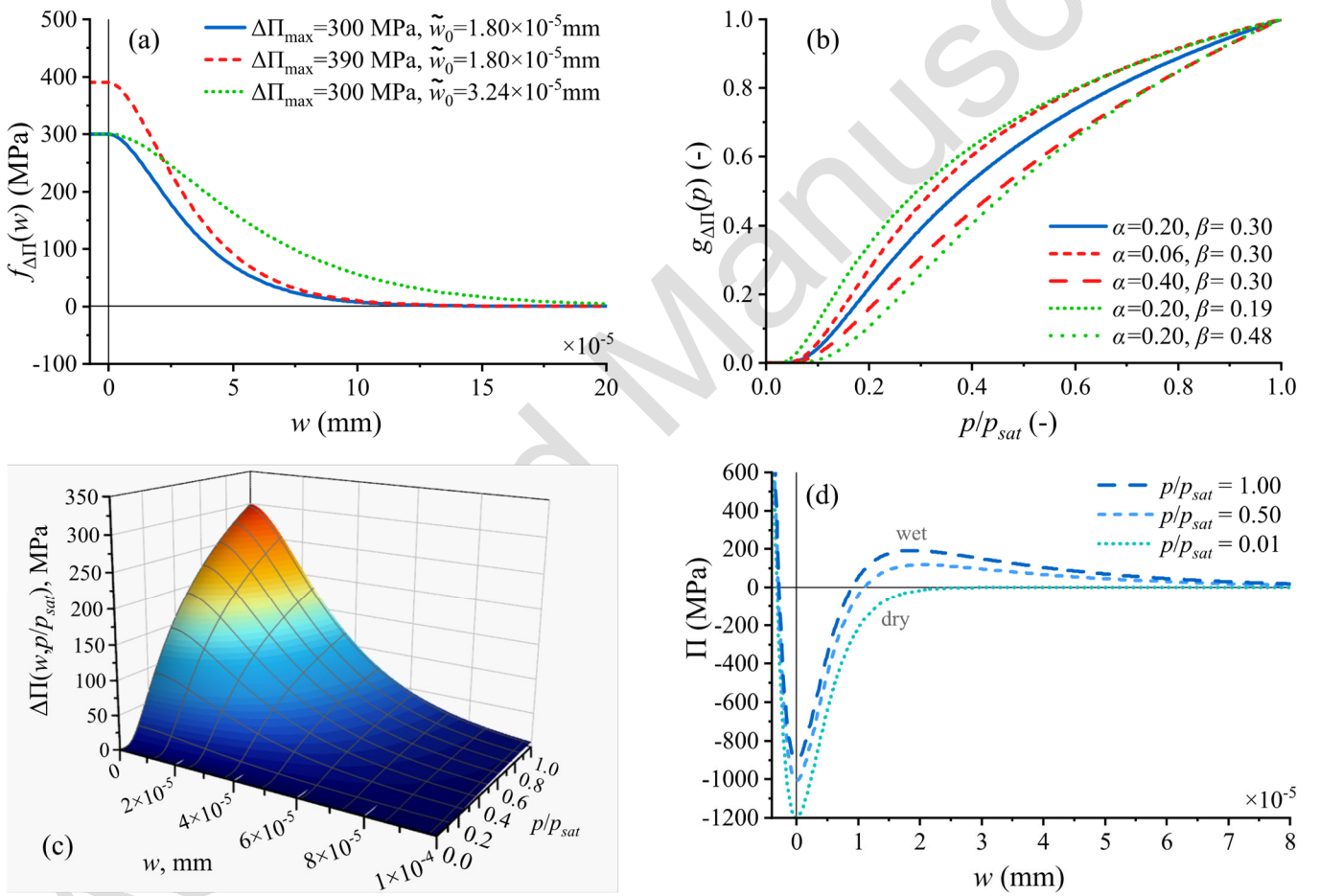
329   surfaces.

330
331   Fig. 7. Environment-induced disjoining pressure as a function of (a) separation and (b) relative partial pressure; (c) the $\Delta\Pi$
332   surface in the $w-p$ space with $\Delta\Pi_{max} = 300\,\text{MPa}$, $\tilde{w}_0 = 1.8 \times 10^{-5}\,\text{mm}$, $\alpha = 0.2$, and $\beta = 0.3$; and (d) the total disjoining
333   pressure Eq. (8) with $\Pi_{0,max} = 1200\,\text{MPa}$ and $w_0 = 3.18 \times 10^{-6}\,\text{mm}$.

334
335
336
337
338

5. MASS TRANSPORT ALONG THE CRACK

The effect of sorption on crack growth is contingent upon the accessibility of sorptive species near the crack tip. This is controlled by the species transport along the crack path and is expected to trail behind as the crack propagates faster. The spatiotemporal evolution of species concentration in turn impacts the resultant disjoining pressure (Fig. 2) and further the K_{Ie} and the crack velocity, thus forming a two-way coupling. Resolving species transport is therefore essential to the proposed SFFT model for capturing the full SCG behavior. Below we develop a generic transport model to capture the most basic features of gas flow in cracks. A one-dimensional treatment is adopted, assuming that gas migrates towards the crack tip along the crack path (x-direction in Fig. 3a). The steady-state solution with respect to the crack tip of the transport model will be sought, considering crack propagation velocities in stages I and II are typically slow (of order 10^{-4} m/s or less). In other words, we examine the steady-state crack propagation scenarios at each K_{Ia} value during an SCG test without considering the short transient stages between K_{Ia} increments.

Consider a small segment δx along the crack with respect to the $x-y$ coordinate fixed in space (Fig. 8), the number of moles of sorptive species must be conserved:

$$\delta n(x,t)Lw(x)\delta x = J(x,t)Lw(x)\delta t - J(x+\delta x,t)Lw(x+\delta x)\delta t \tag{13}$$
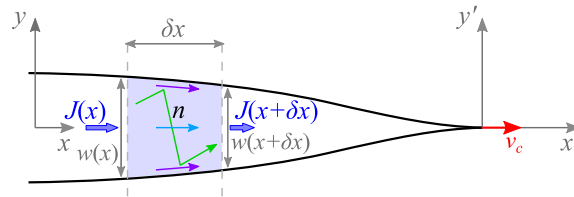

Fig. 8. Schematic of gas transport along propagating crack. The light blue, purple, and green arrows represent, respectively, bulk gas (viscous) flow, surface diffusion, and Knudsen flow as examples of the transport mechanisms.

where L is the depth of the crack in the z direction; n is the molar concentration with a unit of mole per volume; J is the molar flux with a unit of mole per unit area per unit time; and w is the crack

360   opening treated here as a known. By Taylor expansion of $J(x+\delta x)$ and $w(x+\delta x)$, and taking the limit

361   of $\delta x \to 0$ and $\delta t \to 0$, Eq. (13) can be rewritten as

362
$$\frac{\partial n(x,t)}{\partial t} = -\frac{1}{w(x,t)}\frac{\partial}{\partial x}\left(w(x,t)J(x,t)\right) \tag{14}$$

363   For an ever-expanding domain (i.e., a moving crack tip), "steady state" only makes sense for an

364   observer that moves together with the crack tip, i.e., the near-tip species concentration profile stops

365   evolving for that observer. Let us therefore define a new coordinate system $x'-y'$ that moves according

366   to $x' = x - v_c t$ and $y' = y$ (Fig.   8).   It   follows $n_t(x,t) = n_t(x',t) - v_c n_{x'}(x',t)$ and

367    $(w(x)J(x,t))_x = (w(x)J(x,t))_{x'}$, where $(\cdot)_t = \partial(\cdot)/\partial t$, $(\cdot)_x = \partial(\cdot)/\partial x$, and $(\cdot)_{x'} = \partial(\cdot)/\partial x'$. Thus the molar

368   balance in Eq. (14) can be written in the $x'-y'$ coordinate as

369
$$\frac{\partial n(x',t)}{\partial t} = v_c \frac{\partial n(x',t)}{\partial x'} - \frac{1}{w(x',t)}\frac{\partial}{\partial x'}(w(x',t)J(x',t)) \tag{15}$$

370   Examining the steady-state condition $\partial(\cdot)/\partial t = 0$ of Eq. (15) gives the following ordinary differential

371   equation:

372
$$v_c \frac{\partial n}{\partial x'} = \frac{1}{w}\frac{\partial}{\partial x'}(wJ) \tag{16}$$

373   It relates the steady-state profiles $n(x')$, $w(x')$, and $J(x')$ at given boundary conditions. Without losing

374   generality, the species transport may be depicted by

375
$$J(x) = -D\frac{\partial n}{\partial x} \tag{17}$$

376   where D is a transport coefficient. At chemical equilibrium, the partial pressure (p), concentration (n),

377   and chemical potential (μ) of the sorptive species are one-to-one related through the equation of state.

378   Thus, D can be re-written in terms of permeability for viscous and Knudsen flow or diffusivity for

379   molecular and surface diffusion. This preserves the generality of the model and enables more detailed

380   examinations of the various transport mechanisms in future studies. Substitution of Eq. (17) in Eq. (16)

381   gives

$$382 \qquad v_c \frac{\partial p}{\partial x'} = -\frac{1}{w}\frac{\partial}{\partial x'}\left(wD\frac{\partial p}{\partial x'}\right) \qquad (18)$$

383   where the ideal gas law ($p = nRT$) and isothermal process ($dT = 0$) are assumed. The steady-state

384   pressure distribution $p(x')$ can be obtained by numerically solving Eq. (18) together with the $\Pi - w$

385   system introduced in the previous section. This is however numerically taxing considering solving the

386   $\Pi - w$ system already requires an iterative scheme. Alternatively, an explicit analytical expression of

387   $p(x')$ can be obtained by assuming $\partial w / \partial x' \approx 0$ and constant D in Eq. (18). This compromise

388   significantly eases the global solution scheme and permits quantitative studies of the first-order

389   behaviors of the proposed SFFT model. With these simplifying assumptions, Eq. (18) can be

390   immediately integrated under the boundary conditions of $p = p_0$ at the crack mouth ($x' = -a$) and

391   $J = v_c n$ at crack tip ($x' = 0$) to give:

$$392 \qquad p(x') = p_0 \exp\left(-\frac{v_c}{D}(x' + a)\right) \qquad (19)$$

393   where p_0 is the partial gas pressure in the environment outside the crack.

394   In reality, it is expected that gas transport from crack mouth to tip involves multiple mechanisms

395   each of which control the transport rate at different crack width (Fig. 9a). For example, bulk gas flow

396   may be dominant at large crack openings (from M to A in Fig. 9b) because of the w^2 – dependency of

397   its diffusivity or permeability D (Wu et al., 2015). As the crack tip is approached and the crack opening

398   narrows, viscous flow rapidly diminishes, and a secondary transport mechanism gains dominance to

399   permit molecular diffusion in nanometer spaces (from B to T in Fig. 9b). This specific transport

400 mechanism near crack tip is currently not well understood. Lawn (1974) argues that molecular collisions

401 with the crack walls, known as Knudsen diffusion, is the mechanism of near-tip transport. Wiederhorn

402 (1967) postulated that there exists a near-tip region, the so called "boundary layer", that is always

403 inaccessible to bulk gas flow. Water molecules can only migrate through the gas mixture in this region

404 via Fickian diffusion at the same rate that they are chemically consumed at the crack tip. Contrarily,

405 experimental data from glass SCG at different temperatures by Crichton et al. (1999) does not support

406 the dominance of Fickian diffusion nor Knudsen diffusion in the boundary layer by comparing the

407 anticipated versus the observed temperature-dependence of the stage-II crack velocity. They suggested

408 surface diffusion is a plausible mechanism to explain the temperature-dependence, but at the same time

409 also suggested that more complex mechanisms or their combinations could be responsible. An ongoing

410 research effort at the Lawrence Berkeley National Laboratory is aimed at providing better understanding

411 of these complex transport mechanisms in glass cracks at nano-scale.

412 Given the lack of a comprehensive transport model that captures the various mechanisms along the

413 crack, we opt for a simplified, segmented, analytical steady-state pressure profile to account for the

414 multi-regime transport of species in complementary to the single-regime model in Eq. (19). Particularly,

415 species transport is assumed to take form of rapid bulk flow for crack width $w > w_{th}$ (from M to C in Fig.

416 9c) where the pressure drop is negligible and slow diffusion for $w_{th} < w$ (from C to T in Fig. 9c) where

417 the pressure profile is similarly described by Eq. (19):

418
$$\begin{cases} p(x') = p_0 & ; \quad \forall x' \,|\, w(x') > w_{th} \\ p(x') = p_0 \exp\left(-\frac{v_c}{D}(x'+d)\right) & ; \quad \forall x' \,|\, w(x') \le w_{th} \end{cases} \tag{20}$$

419 where w_{th} is a threshold crack width to be discussed later; d is defined such that $w(x') > w_{th}$ for all

420 $x' < -d$. This dual-regime model (Fig. 9c) is conceptually similar to Wiederhorn's boundary layer

421   model (Wiederhorn, 1967). In essence, the only difference between the single-regime flow Eq. (19) and

422   the dual-regime flow Eq. (20) is that d is fixed at $d = a$ in the former, but becomes a variable related to

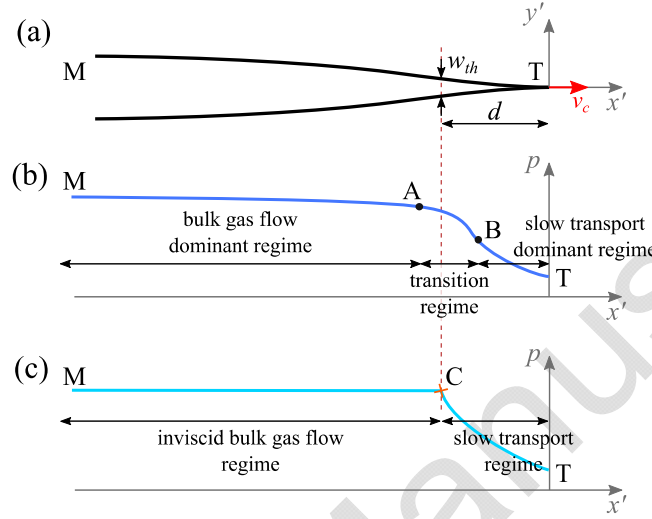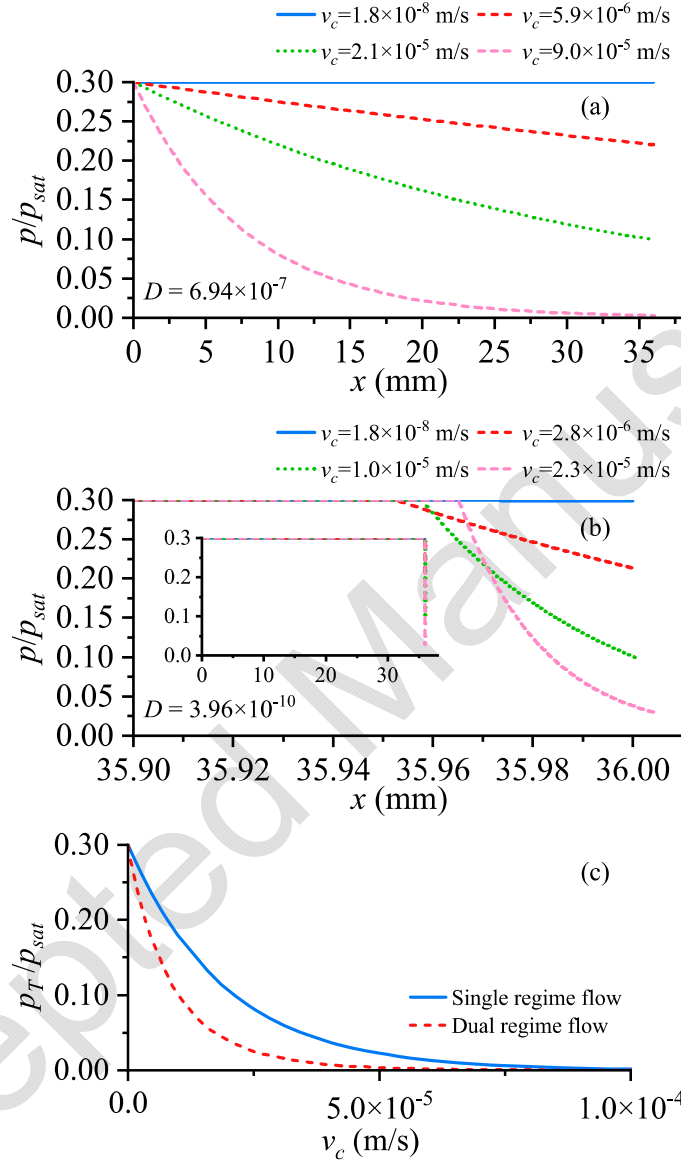423 w_{th} in the latter.

424
425   Fig. 9. Schematic of the near tip crack profile (a), the realistic pressure profile in nano-spaces (b) inspired by Cihan et al.
426   (2021), and the approximated dual-regime pressure profile (c).

427   The threshold crack width w_{th} may be selected based on the Knudsen number, $\mathrm{Kn} = \lambda / w$, where λ

428   is the mean free path of the gas (Lawn, 1974). $\mathrm{Kn} \ll 1$ suggests transport dominated by viscous flow,

429   while $\mathrm{Kn} \gg 1$ suggests transport by slower diffusion mechanisms (Choi et al., 2001). Therefore, it is

430   reasonable to define $w_{th} = \lambda / \mathrm{Kn}_0$ where Kn_0 marks the transition point taken to be $1/3$ here, well

431   within the range of $0.01 < \mathrm{Kn}_0 < 1$ recommended by Lawn (1974). The experiments of glass SCG by

432   Wiederhorn (1967) is performed in a nitrogen-water vapor environment at room temperature and

433   atmospheric pressure, based on which the mean free path can be approximated as $\lambda \approx 7 \times 10^{-8} \mathrm{m}$ (Bird et

434   al., 2006; Chapman and Cowling, 1990; Jennings, 1988).

435   Fig. 10a and b plot the steady-state vapor pressure profiles at different crack velocity for crack

436   length $a = 36\mathrm{mm}$ and ambient humidity $\mathrm{RH}_0 = p_0 / p_{sat} = 0.3$. The dual-regime flow based on the

437   current estimation of w_{th} predicts that the slow molecular diffusion only gets activated extremely close

438 (tens of μm) to the crack tip. Both models predict exponential decay of crack-tip vapor concentration

439 with increasing velocity (Fig. 10c).

440
441 Fig. 10. Steady-state vapor partial pressure profile based on the (a) single-regime model Eq. (19), and (b) dual-regime model
442 Eq. (20) at different crack velocities. (c) Crack-tip pressure exponentially decreases as crack velocity increases. The model
443 parameters used are those of Table 3.

6. SOLUTION SCHEME

445 Our SFFT model specialized for glass SCG is now complete with fracture mechanics Eqns. (1) and

446 (2), crack kinetics Eq. (7), surface force model Eqns. (9) and (10), and transport model Eq. (19) or (20).

447   This section seeks the solution of the system subject to stress, $\sigma(t)$, over domain $x \in [0, a]$, and at each

448   point in time t_k. Over each time increment $(t_k, t_k + \Delta t_k)$, the crack length is updated based on

449
$$a(t_k + \Delta t_k) = a(t_k) + v_c(t_k)\Delta t_k \tag{21}$$

450   where Δt_k is initially set to $0.05\,\text{sec}$. It is reduced if the relative error at t_k is small and increased if the

451   relative error is large, within the range of $0.02\,\text{sec} - 1\text{sec}$.

452   For spatial discretization, nodes are distributed along the crack at the mid-plane, permitted by the

453   one-dimensional nature of the problem. The crack is divided by N nodal points located at $(x_1, x_2, ..., x_N)$

454   that are densely distributed ($\sim$ every 6 nm) near the crack tip and coarsely distributed ($\sim$ every 70 μm)

455   close to the crack mouth. This is because of the nature of surface forces: they take large magnitudes and

456   vary dramatically at short separations, then diminish quickly as the separation increases, making the

457   system extremely non-linear near the crack tip. With this discretization, the unknown vectors $\mathbf{p}$, $\mathbf{w}$, and

458    $\mathbf{\Pi}$ are defined as $p_i = p(x_i)$, $w_i = w(x_i)$, and $\Pi_i = \Pi(x_i)$, respectively.

459   For the modularity of the numerical scheme, the equations are grouped in three subsystems: **S1**) the

460   fluid transport subsystem, Eq. (19) or (20); **S2**) the fracture mechanics $\Pi - w$ subsystem, Eqns. (1), (2),

461   (9), and (10); and **S3**) the crack propagation subsystem, Eq. (7). They are then iteratively coupled at the

462   global level to search for a solution that simultaneously satisfies all the underlying equations.

463   For S1, the transport models in Eqns. (19) and (20) provide explicit solution at all points. In discrete

464   form, the nodal pressure described by these models are, respectively,

465
$$p_i = p_0 \exp\left(-\frac{v_c}{D}x_i\right) \tag{22}$$

466   and

467

$$468 \qquad p_i = \begin{cases} p_0 & ; \quad \forall x_i \mid w(x_i) > w_{th} \\ p_0 \exp\left(-\dfrac{v_c}{D}(x_i - a + d)\right) & ; \quad \forall x_i \mid w(x_i) \leq w_{th} \end{cases} \qquad (23)$$

469 x_i is the coordinate of node i in the coordinate system set at the crack mouth, consistent with that used

470 for the fracture mechanics solution (Fig. 3). For S2, an iterative method is required to solve the $\Pi - w$

471 equations at fixed p profiles. Consistent Π and w profiles together with the resultant K_{Ie} are obtained

472 by following the solution method of Planas and Elices (1991), while taking advantage of the analytical

473 solutions made available by Tada et al. (2000) (Appendix A). For S3, Eq. (7) simply inputs an effective

474 stress intensity and outputs the resultant crack velocity.

475 The global coupling of S1, S2, and S3 is achieved through a partitioned Newton-Raphson method.

476 This method follows the multi-level Newton method of Kim et al. (2003). At local level, S1, S2, and S3

477 are solved separately and independently. It is important to distinguish the global unknowns as the

478 guessed inputs and the response of each subsystem to its pertaining guessed inputs as the local outputs.

479 The global unknowns are defined here as the partial pressure of the adsorptive fluid, $\mathbf{p}$; the crack

480 opening, $\mathbf{w}$; the effective stress intensity factor at the crack tip, K_{Ie}; and the crack velocity, v_c. We

481 shall then denote the solution to the fluid profile in response to guess values of crack opening and crack

482 velocity by $\hat{\mathbf{p}}(\mathbf{w}, v_c)$, solved by S1; the crack opening and effective stress intensity in response to guess

483 values of fluid state profile by $\hat{\mathbf{w}}(\mathbf{p})$ and $\hat{K}_{Ie}(\mathbf{p})$, solved by S2; and the crack propagation velocity in

484 response to a guess value of stress intensity factor by $\hat{v}_c(K_{Ie})$, solved by S3. The coupling is achieved

485 by directing the global residual to zero in an iterative manner.

486 The vector of global unknowns is constructed as

$$\mathbf{u} = \begin{bmatrix} \mathbf{p} \\ \mathbf{w} \\ K_{Ie} \\ v_c \end{bmatrix} \qquad (24)$$

487

488   The global residual is defined as

489
$$\mathbf{R} = \begin{bmatrix} \mathbf{p} - \hat{\mathbf{p}}(\mathbf{w}, v_c) \\ \mathbf{w} - \hat{\mathbf{w}}(\mathbf{p}) \\ K_{Ie} - \hat{K}_{Ie}(\mathbf{p}) \\ v_c - \hat{v}_c(K_{Ie}) \end{bmatrix} \qquad (25)$$

490   where $\mathbf{p}$, $\mathbf{w}$, K_{Ie}, and v_c are the values of the unknowns at the current iteration. The global solution

491   that simultaneously satisfies S1, S2, and S3 can be found by iteratively marching towards $\mathbf{R} = \mathbf{0}$ via the

492   Newton-Raphson method. In each iteration, the correction to $\mathbf{u}$, $\delta\mathbf{u}$, can be obtained from

493    $\delta\mathbf{u} = -\mathbf{J}^{-1}(\mathbf{u}) \cdot \mathbf{R}(\mathbf{u})$ where $\mathbf{J}$ is the global Jacobian matrix defined as:

494
$$\mathbf{J} = \frac{\partial \mathbf{R}}{\partial \mathbf{u}} = \begin{bmatrix} \dfrac{\partial\left(\mathbf{p} - \hat{\mathbf{p}}(\mathbf{w}, v_c)\right)}{\partial \mathbf{p}} & \dfrac{\partial\left(\mathbf{p} - \hat{\mathbf{p}}(\mathbf{w}, v_c)\right)}{\partial \mathbf{w}} & \dfrac{\partial\left(\mathbf{p} - \hat{\mathbf{p}}(\mathbf{w}, v_c)\right)}{\partial K_{Ie}} & \dfrac{\partial\left(\mathbf{p} - \hat{\mathbf{p}}(\mathbf{w}, v_c)\right)}{\partial v_c} \\[4mm] \dfrac{\partial\left(\mathbf{w} - \hat{\mathbf{w}}(\mathbf{p})\right)}{\partial \mathbf{p}} & \dfrac{\partial\left(\mathbf{w} - \hat{\mathbf{w}}(\mathbf{p})\right)}{\partial \mathbf{w}} & \dfrac{\partial\left(\mathbf{w} - \hat{\mathbf{w}}(\mathbf{p})\right)}{\partial K_{Ie}} & \dfrac{\partial\left(\mathbf{w} - \hat{\mathbf{w}}(\mathbf{p})\right)}{\partial v_c} \\[4mm] \dfrac{\partial\left(K_{Ie} - \hat{K}_{Ie}(\mathbf{p})\right)}{\partial \mathbf{p}} & \dfrac{\partial\left(K_{Ie} - \hat{K}_{Ie}(\mathbf{p})\right)}{\partial \mathbf{w}} & \dfrac{\partial\left(K_{Ie} - \hat{K}_{Ie}(\mathbf{p})\right)}{\partial K_{Ie}} & \dfrac{\partial\left(K_{Ie} - \hat{K}_{Ie}(\mathbf{p})\right)}{\partial v_c} \\[4mm] \dfrac{\partial\left(v_c - \hat{v}_c(K_{Ie})\right)}{\partial \mathbf{p}} & \dfrac{\partial\left(v_c - \hat{v}_c(K_{Ie})\right)}{\partial \mathbf{w}} & \dfrac{\partial\left(v_c - \hat{v}_c(K_{Ie})\right)}{\partial K_{Ie}} & \dfrac{\partial\left(v_c - \hat{v}_c(K_{Ie})\right)}{\partial v_c} \end{bmatrix} \qquad (26)$$

495   Upon simplification, one has

$$
\mathbf{J} = \begin{bmatrix}
\mathbf{I} & -\dfrac{\partial \hat{\mathbf{p}}}{\partial \mathbf{w}} & \mathbf{0} & -\dfrac{\partial \hat{\mathbf{p}}}{\partial v_c} \\[2ex]
\hline
-\dfrac{\partial \hat{\mathbf{w}}}{\partial \mathbf{p}} & \mathbf{I} & \mathbf{0} & \mathbf{0} \\[2ex]
\hline
-\dfrac{\partial \hat{K}_{Ie}}{\partial \mathbf{p}} & \mathbf{0} & 1 & 0 \\[2ex]
\hline
\mathbf{0} & \mathbf{0} & -\dfrac{\partial \hat{v}_c}{\partial K_{Ie}} & 1
\end{bmatrix}
\tag{27}
$$

A schematic of this partitioned Newton-Raphson scheme is presented in Fig. 11 for clarity.

The derivatives in Eq. (27) can be computed from Eq. (7), Eqns. (A.6) and (A.7) of Appendix A, and Eq. (22) or (23) depending on the choice of the transport model:

$$
\frac{\partial \hat{v}_c}{\partial K_{Ie}} = \frac{v_0 \kappa_0}{RT} \exp\!\left(-\frac{Q_0}{RT}\right) \cosh\!\left(\frac{\kappa_0 K_{Ie}}{RT}\right)
\tag{28}
$$

$$
\frac{\partial \hat{w}_i}{\partial p_j} = c_{\Pi,ik} \frac{\partial \hat{\Pi}_k}{\partial p_j} \approx c_{\Pi,ik} \frac{\partial \Pi_k}{\partial p_j}
\tag{29}
$$

$$
\frac{\partial \hat{K}_{Ie}}{\partial p_j} = k_{I\Pi,k} \frac{\partial \hat{\Pi}_k}{\partial p_j} \approx k_{I\Pi,k} \frac{\partial \Pi_k}{\partial p_j}
\tag{30}
$$

$$
\frac{\partial \hat{p}_i}{\partial w_j} = \frac{\partial \hat{p}_i}{\partial d} \frac{\partial d}{\partial w_j} \approx 0
\tag{31}
$$

$$
\frac{\partial \hat{p}_i}{\partial v_c} = -\frac{x_i}{D} p_0 \exp\!\left(-\frac{v_c}{D} x_i\right)
\tag{32}
$$

for single-regime flow, and

$$506 \qquad \frac{\partial \hat{p}_i}{\partial v_c} = \begin{cases} 0 & ; \quad \forall x \mid w(x) > w_{th} \\ -\dfrac{x_i - a + d}{D} p_0 \exp\left(-\dfrac{v_c}{D}(x_i - a + d)\right) & ; \quad \forall x \mid w(x) \le w_{th} \end{cases} \qquad (33)$$
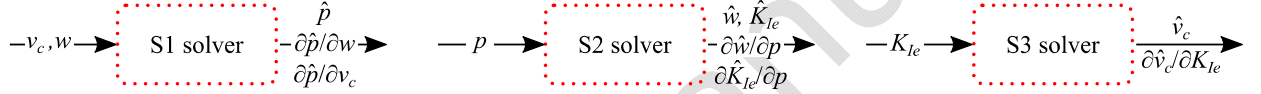
507   for dual-regime flow.

508   The errors are defined as

$$509 \qquad \varepsilon_p = \left| \frac{\delta p_i}{p_i} \right|, \ \varepsilon_w = \left| \frac{\delta w_i}{w_i} \right|, \ \varepsilon_{K_{Ie}} = \left| \frac{\delta K_{Ie}}{K_{Ie}} \right|, \text{ and } \varepsilon_{v_c} = \left| \frac{\delta v_c}{v_c} \right| \qquad (34)$$

510   The iterations continue until the maximum of the four errors falls within a tolerance of 10^{-5}.
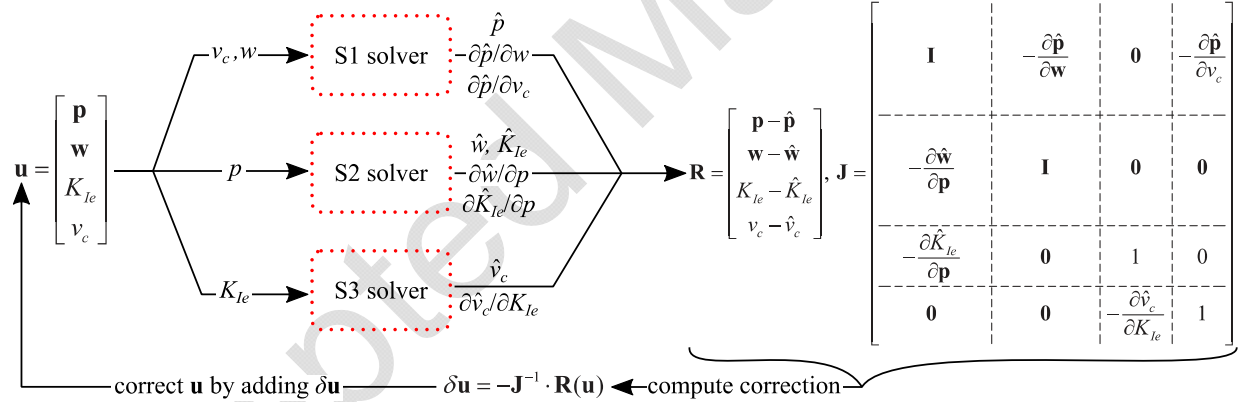

511
512   Fig. 11. A schematic of (a) the inputs and outputs of the S1, S2, and S3 solvers; and (b) the partitioned Newton-Raphson
513   scheme to seek solutions satisfying all subsystems.

514   Note that the length of the slow transport regime d varies continuously as the crack opens or closes,

515   while the numerical representation of the crack opening $\mathbf{w}$ is discrete and does not allow smooth

516   variation of d. Therefore, a linear interpolation for the value of $w(x)$ between two nodes is adopted to

517   allow smooth variation of d. Consequently, the derivative $\partial d / \partial \mathbf{w}$ cannot be effectively computed

518   without explicit expression of d. This term is expected to be small anyway given the initial guess for $\mathbf{w}$

519   is close to the solution. The derivative in Eq. (31) is thus approximated by zero. In addition, the $\partial \hat{\mathbf{\Pi}} / \partial \mathbf{p}$

520   term in Eq. (29) must be approximated since the $\Pi - w$ system is implicitly solved without being

521   written in terms of $\mathbf{p}$. Two versions of the implementation were tested, one with $\partial\hat{\mathbf{\Pi}}/\partial\mathbf{p} \approx (\partial\hat{\mathbf{\Pi}}/\partial\mathbf{p})_{\hat{\mathbf{w}}}$

522   and $\partial\hat{\mathbf{w}}/\partial\mathbf{p}$ given by Eq. (29), and the other with $\partial\hat{\mathbf{w}}/\partial\mathbf{p} \approx \mathbf{0}$. The second approximation yielded better

523   convergence and was adopted in the final implementation. Finally, a proper initial guess is required to

524   start the search for the solution at each time t_{k+1} due to the highly nonlinear nature of the problem. A

525   robust initial guess algorithm is described in Appendix B.

7. PERFORMANCE OF THE FRAMEWORK

527   This section compares the SFFT prediction against Wiederhorn's SCG data (Fig. 12) to validate the

528   underlying hypotheses depicted in Fig. 1.

7.1. Model calibration

530   We shall calibrate the least coupled parts of the model first. The intrinsic material properties

531   including the elastic parameters, in-vacuum surface force, and the reaction kinetic parameters are

532   therefore calibrated first here. These parameters are expected to control the in-vacuum stage-III SCG

533   response.

534   The standard Young's modulus of soda-lime glass is 70 GPa (572-1, 2012) while the reported ones

535   in literatures vary between 50 GPa and 85 GPa (Meyland et al., 2021). A Poisson ratio in the range of

536    $0.2 \sim 0.3$ has been reported in some studies (Li and Wei, 2020; Meyland et al., 2021; Xu et al., 2017).

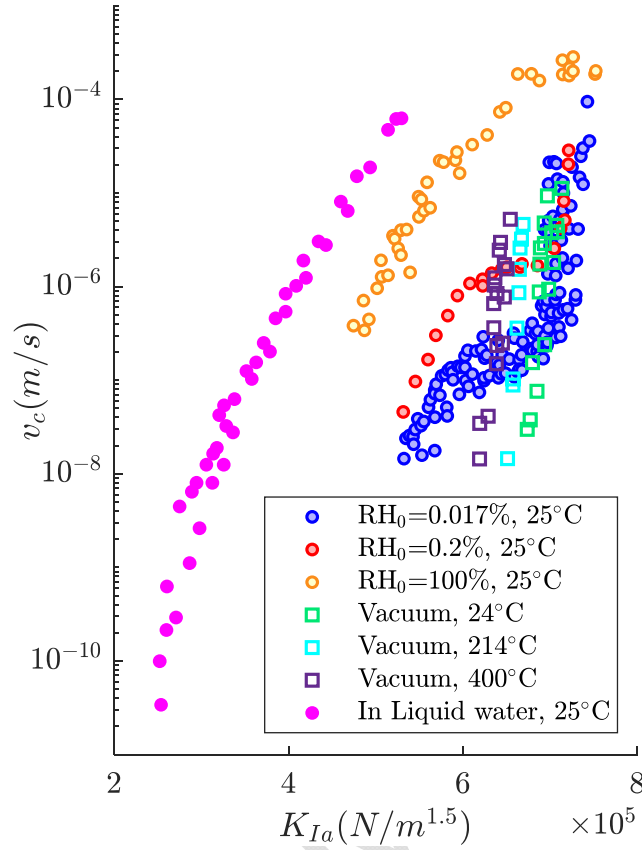537   Within this ballpark, the selected elastic parameters are shown in Table 1.

538
539 Fig. 12. Data for crack propagation in soda-lime glass at 25°C and different relative humidity (Wiederhorn, 1967; Wiederhorn
540 et al., 1980), open circles; at different temperatures at 24°C, 214°C, and 400°C in vacuum (Wiederhorn, 1974), squares; and in
541 liquid water (Wiederhorn and Bolz, 1970), filled circles.

542   Two types of data are adopted to calibrate the Π_0 parameters. The first data is surface energy for

543 soda-lime glass measured by Wiederhorn (1969) at near room temperature in an environment with

544 background nitrogen gas (inert) as $\gamma = 3.82\,\mathrm{J/m^2}$. This measurement in inert gas can estimate the area

545 underneath the $\Pi_0 - w$ curve, in absence of sorptive species (Gdoutos, 2020). For the selected Π_0

546 expression Eq. (9), this area is $\gamma = \Pi_{0,\max} w_0$. The second data is the SFA measurements between a glass

547 sphere in air (Yaminsky and Stewart, 2003), scaled by a factor of 912.6 such that the area underneath

548 this data matches the surface energy measurement. Parameters $\Pi_{0,\max}$ and w_0 are then selected (Table 1)
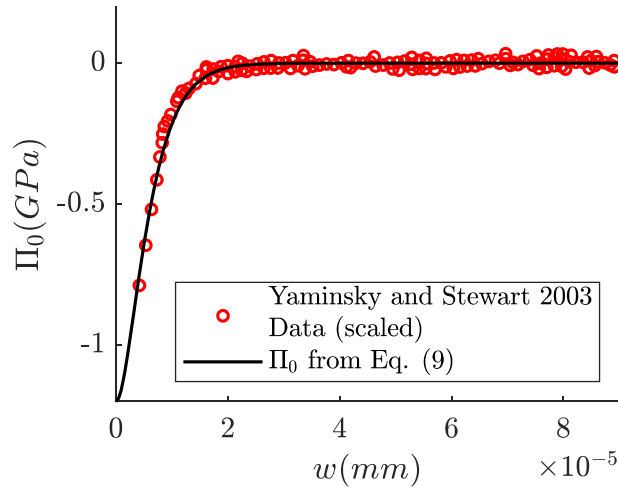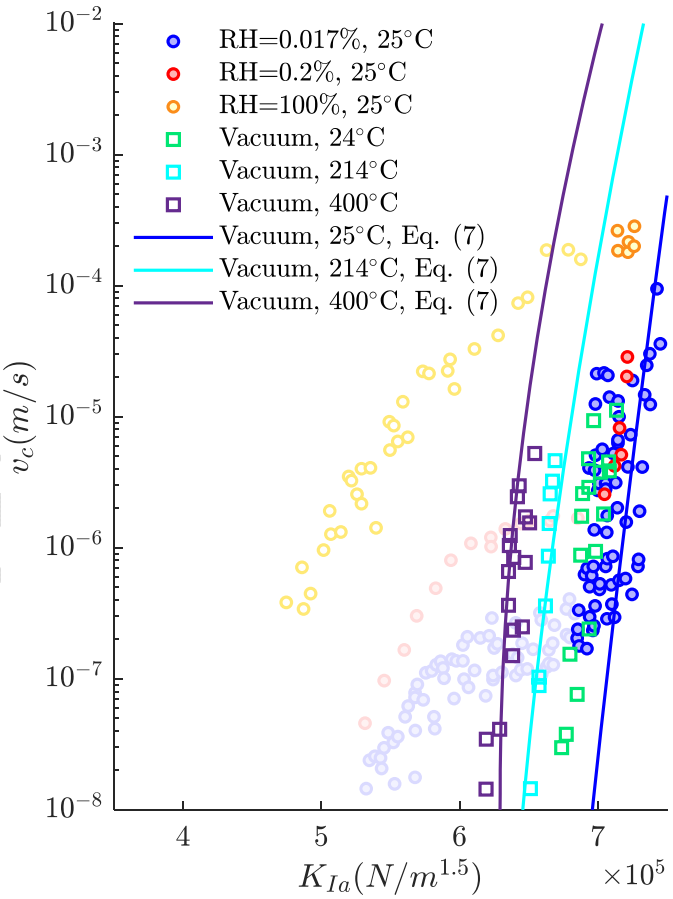
549 to match this data (Fig. 13).

Fig. 13. Calibrated in-vacuum surface force ($\Pi_{0,\max} = 1200\text{MPa}$ and $w_0 = 3.1833 \times 10^{-6}\text{mm}$) vs. SFA measurements. A constant multiplying factor is applied to the SFA data to roughly match the area under this curve with the surface energy measurement of $\gamma = 3.82\text{J/m}^2$. The Π_0 data is converted from F/R data multiplied by 912.6.

The reaction kinetic parameters are calibrated against the in-vacuum $v_c - K_{Ia}$ data. At relatively large K_{Ia} values, the $K_{Ie} - K_{Ia}$ relation becomes linear (see Fig. 6) and so does the $\log(v_c) - K_{Ie}$ relation (Eq. (7)). Combining the two gives a linear one-to-one correspondence between K_{Ia} and v_c at high K_{Ia} levels. Note that there are infinite combinations of v_0, Q_0, and κ_0 to match a linear set of $\log(v_c) - K_{Ia}$ data. Such arbitrariness can be removed by considering the temperature dependence of the crack kinetics. Specifically, the same set of v_0, Q_0, and κ_0 should capture the in-vacuum $v_c - K_{Ia}$ curves obtained at different temperatures, assuming the Arrhenius term in Eq. (7) outweighs the temperature dependence of the elastic parameters and in-vacuum surface forces. Fig. 14 plots soda-lime glass $v_c - K_{Ia}$ data obtained at 24°C, 214°C, and 400°C (Wiederhorn, 1974) based on which the kinetic parameters v_0, Q_0, and κ_0 are calibrated (Table 1). Their values are the same orders of magnitude as those presented in Wiederhorn (1974).

567   Table 1. Model parameters that control stage III SCG behavior

Parameter	Unit	Values
Elasticity		
E	[MPa]	50000
ν	[-]	0.2
In-vacuum surface force		
w_0	[mm]	3.1833×10^{-6}
$\Pi_{0,max}$	[MPa]	1200
Crack propagation reaction		
v_0	[mm/s]	3.303×10^5
Q_0	[J/mol]	1.31×10^5
κ_0	[m$^{2.5}$/mol]	0.24

568
569
570

571
572   Fig. 14. Calibration of reaction rate parameters v_0, Q_0, and κ_0 against SCG data at three temperatures, 25°C, 214°C, and
573   400°C in vacuum. The irrelevant data are faded for clarity.

574   The model is now fully calibrated for the in-vacuum condition. We now move on to determine

575   parameters that control the environmental dependency, specifically the environment-induced disjoining

576   pressure $\Delta\Pi$ and the pressure profile $p(x)$. The former is expected to affect the strength reduction in

577   stage I, and the latter limits the rate of crack propagation in stage-II SCG.

578   In Eqns. (10), (11), and (12), parameters $\Delta\Pi_{max}$ and $\tilde{w}_0$ control the dependence of $\Delta\Pi$ on the crack

579   opening and parameters α and β independently control the dependence of $\Delta\Pi$ on the partial pressure

580   of the adsorbate. AFM measurements in glass-liquid water system (Acuña and Toledo, 2008) provides a

581   benchmark for the shape of the $\Delta\Pi - w$ relation at $p = p_{sat}$ which allows the determination of $\tilde{w}_0$ (Fig.

582   15). The area underneath $\Delta\Pi$ reflects the change of surface energy in presence of water vapor, meaning

583   that $\Delta\Pi_{max}$ can be calibrated based on the reduction of apparent fracture toughness from $RH_0 = 0\%$ to

584   100% (Fig. 16). Finally, parameters α and β in Eq. (12) are tuned to capture the strength reductions at

585    $RH_0 = 0.017\%$, 0.2%, 1%, 10%, and 30% (Fig. 16). These parameters are summarized in Table 2.

586   Table 2. Parameters that control stage I SCG in complement to Table 1.

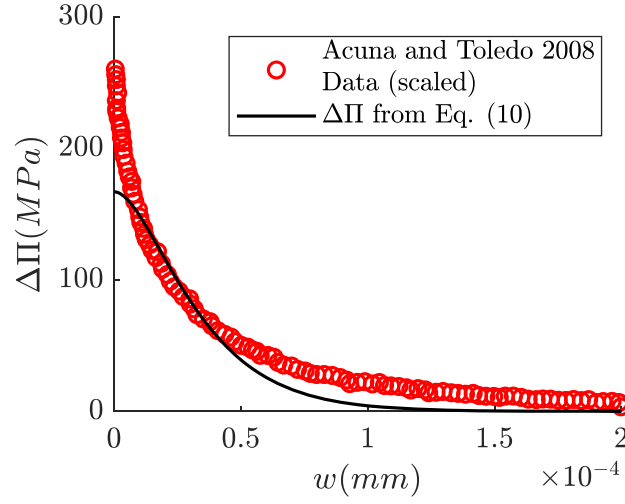| Parameter	Unit	Values
Environment-induced disjoining pressure		
$\tilde{w}_0$	[mm]	1.8×10^{-5}
$\Delta\Pi_{0,max}$	[MPa]	167
α	[-]	0.067
β	[-]	10^{-5}

587

Fig. 15. Calibrated $\Delta\Pi$ with parameters $\tilde{w}_0 = 1.8 \times 10^{-5}$ mm and $\Delta\Pi_{max} = 167$ MPa at $p = p_{sat}$ based on the F/R measurements from AFM (Acuña and Toledo, 2008) scaled by 120.5. The main purpose here is to match the shape via adjusting $\tilde{w}_0$. $\Delta\Pi_{max}$ is determined in Fig. 16.
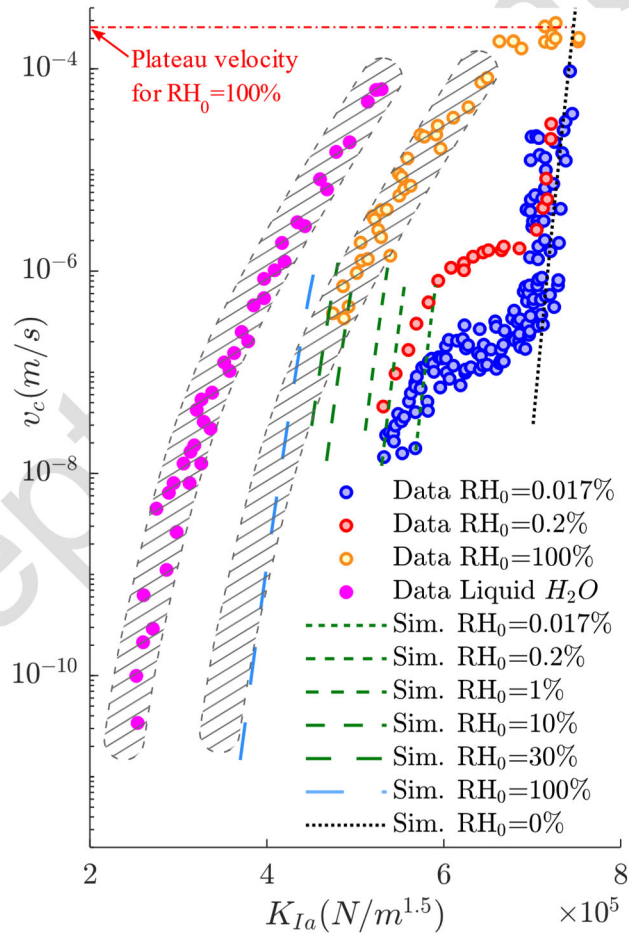

Fig. 16. Measured vs. simulated strength reduction at $RH_0 = 100\%$ with parameters $\Delta\Pi_{max} = 167$ MPa and $\tilde{w}_0 = 1.8 \times 10^{-5}$ mm (light blue coarse-dashed line). The strength reductions for intermediate RH values are captured by selecting $\alpha = 0.067$ and $\beta = 10^{-5}$ (green dashed lines). The cross-hatching is meant as a visual guide for the extension of the

596 $\text{RH}_0 = 100\%$ data based on the data in liquid water. The reason for this extension is to obtain a visual of the $\text{RH}_0 = 100\%$
597 curve at lower velocities for the purpose of calibration.

598 On the transport side, for both $p(x)$ profiles depicted by Eq. (19) and Eq. (20), D is selected such

599 that the adsorbate relative pressure at the crack tip drops to an arbitrary small value (here taken as

600 2×10^{-6}) at the stage-II plateau velocity for the $\text{RH}_0 = 100\%$ case ($v_c = 2.5 \times 10^{-4}\,\text{m/s}$ at

601 $K_{Ia} = 7.44 \times 10^5\,\text{N/m}^{1.5}$ from Fig. 16). The near-tip region length d for the dual-regime flow model is

602 estimated from the in-vacuum crack opening profile at $K_{Ia} = 7.44 \times 10^5\,\text{N/m}^{1.5}$. This gives

603 $d \approx 2.13 \times 10^{-5}\,\text{m}$; i.e., $w < w_{th} = \lambda / \text{Kn}_0$ for $a - 2.13 \times 10^{-5} < x$. The values of D for the two cases are

604 given in Table 3.

605 Table 3. Parameters that control stage II SCG in complement to Table 1 and Table 2.

Parameter	Unit	Values
Single-regime flow		
D	$[\text{m}^2/\text{s}]$	6.94×10^{-7}
Dual-regime flow		
D	$[\text{m}^2/\text{s}]$	3.96×10^{-10}

606 These calibrated D values can be quantitatively compared with some theoretical estimates. In a study

607 of gas transport in shale nanopores, Wu et al. (2015) predicted an equivalent Darcian permeability k (as

608 in $v_{fluid} = -(k / \mu) \partial p / \partial x$) of order $10^{-17}\,\text{m}^2$ for the case of surface diffusion. Conversion of k to D can

609 be made by rewriting $J(x) = -D \partial n / \partial x$ as $v_{fluid} = J / n = -(D / p) \partial p / \partial x$, giving $D = kp / \mu$. A

610 viscosity of order $10^{-5}\,\text{Pa} \cdot \text{s}$ is assumed (Tsilingiris, 2008; Wu et al., 2015), and a pressure of order

611 $< 10^3\,\text{Pa}$ can be assumed considering $O(p_{sat}) = 10^3\,\text{Pa}$ for water vapor. This gives .

612 $O(D_{\text{surf. diff.}}) < 10^{-9}\,\text{m}^2/\text{s}$. for surface diffusion, comparable with the calibrated value of D for dual-

613 regime flow. Similar comparison can be made in the case of Knudsen diffusion (Wu et al., 2015). On the

614 other hand, considering viscous flow in a slit with aperture w, one can derive $D_{\text{bulk flow}} = RTw^2 / 12\mu V_m$

615 for ideal gas. At room temperature, the molar volume of ideal gas is $V_m = 2.45 \times 10^{-2}\,\mathrm{m^3/mol}$. Fig. 5

616 suggests that the crack opening varies from order $10^{-5}\,\mathrm{m}$ to $10^{-8}\,\mathrm{m}$ from the crack mouth to where

617 surface forces are observed. Combining the above gives $O(D_{\text{bulk flow}}) = 10^{-2} \sim 10^{-8}\,\mathrm{m^2/s}$. Note that the

618 estimated $D_{\text{bulk flow}}$ is several orders larger than our calibrated D values (Table 3) and those estimated

619 based on Wu et al. (2015). This justifies our assumption that the pressure drop is negligible in the bulk

620 flow regime up to the transition point (Fig. 9c).

621 **7.2. Model prediction**

622 Using the calibrated parameters in Tables 1, 2, and 3, the SCG curves predicted by the SFFT model

623 for single-regime and dual-regime flow at $\mathrm{RH}_0 = 100\%$ are presented together with experimental data in

624 Fig. 17a. It is exciting to see that, for the first time, the key features of all three stages of SCG and the

625 smooth transition between them are directly predicted by a single mechanistic model. Comparing the

626 two computed SCG curves suggests that the choice of transport model directly impacts the stages I and

627 II SCG behavior. This cannot be observed in existing phenomenological SCG models, since the shape of

628 the whole SCG curve is imposed rather than predicted in these approaches (Charles, 1962; Lawn, 1975).

629 Fig. 17b presents the predicted vapor pressure profiles at different stages of SCG for the dual-regime

630 model. As K_{Ia} increases, the crack opening widens, and the inviscid regime moves closer to the crack

631 tip. However, the simultaneous increase in crack velocity outpaces the crack widening, which results in

632 an overall decrease of fluid concentration at the crack tip. Fig. 17c shows that the disjoining pressure is

633 extremely concentrated near the crack tip and is highly sensitive to the local vapor pressure and thus the

634 crack velocity. This suggests that the introduction of slight repulsive disjoining pressure in the near-tip

635 region can cause significant reduction of the apparent fracture toughness for brittle solids. The profiles

636 plotted in Fig. 17b and c confirm the common speculation that fluid transport is indeed the rate-limiting
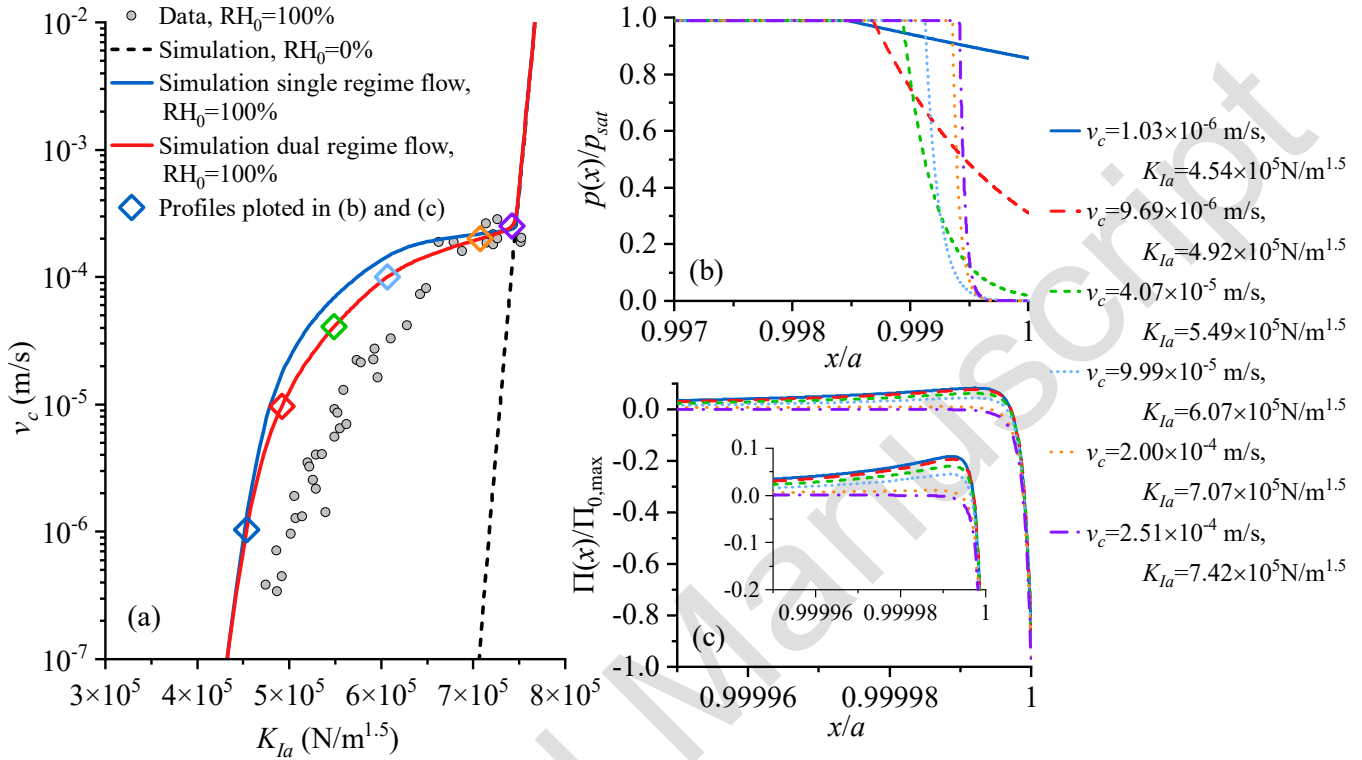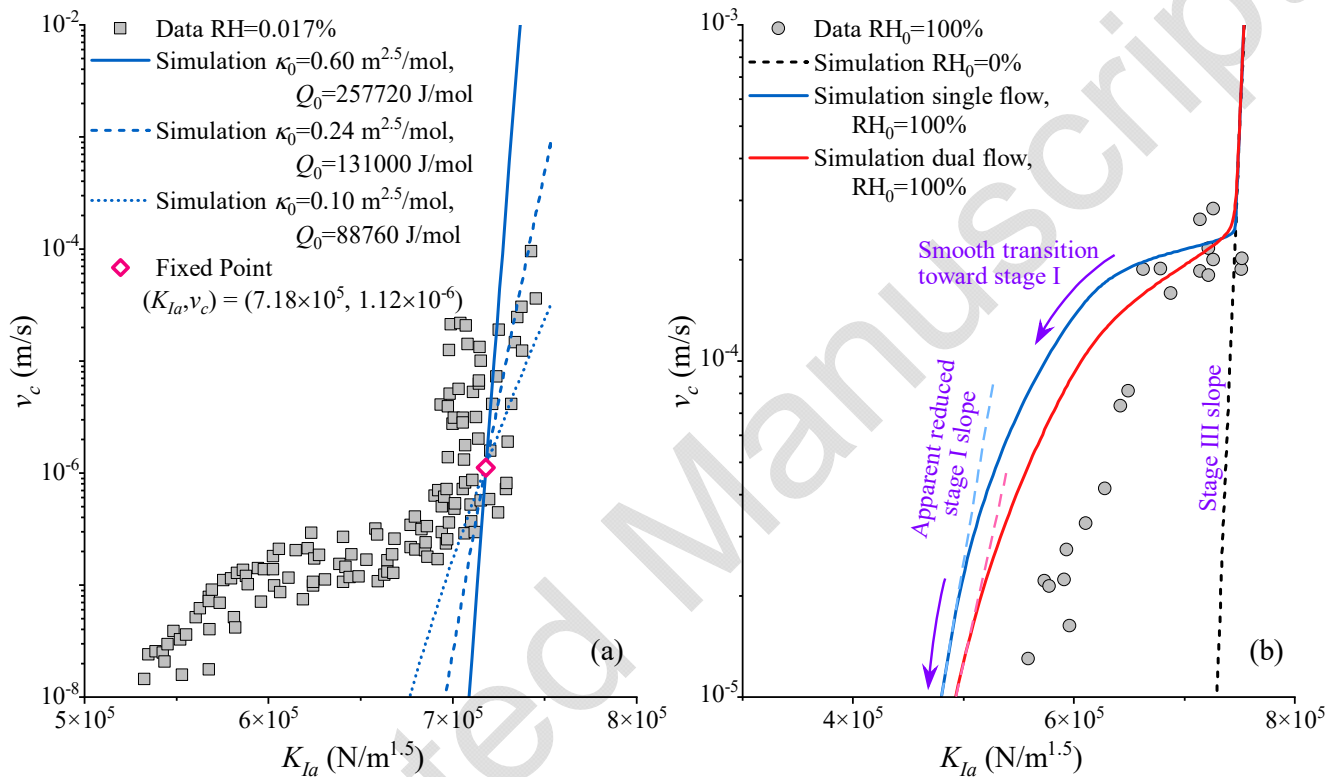
637 mechanism for the stage II of SCG.

638
639 Fig. 17. (a) Measured vs. predicted SCG curves at RH_0 =100% based on single-regime flow and dual-regime flow. (b)
640 Pressure profiles at different stages along the SCG curve depicted by the dual-regime flow model. (c) Disjoining pressure
641 distribution at different stages along the SCG curve.

642 Recalling that the SFFT model was calibrated only for the apparent toughness (where the SCG curve

643 intersects with the $x-$axis) and the plateau velocity (where stages II and III intersects) at $RH_0 = 100\%$,

644 everything in between should be regarded as true predictions. It is observed that the current model

645 generally overestimates the crack velocity in stages I and II, with the dual regime flow model making

646 slightly better prediction. This is because the experimental data suggests the stage-I slope is lower

647 compared to the in-vacuum portion, while the current model predicts the same slopes for stages I and III.

648 We may remediate this through the reaction rate parameters or the fluid transport parameters. Fig. 18a

649 demonstrates that the decrease of κ_0 or Q_0 can reduce the slope of SCG curve in the $\log(v_c) - K_{Ia}$ plane.

650 This implies that the lowered stage-I slope can be accounted for by introducing some environmental

651 dependency on the kinetic parameters. A rigorous proposal of $\kappa_0(p)$ or $Q_0(p)$ requires detailed study

652 of how the energy barrier for bond rupture at the very crack tip lowers under environmental attack,

653 which is beyond the scope of this paper. Alternatively, an apparent slope reduction can be readily

654 observed by cropping out the very low velocity range of the SCG plots (Fig. 18b).

655
656 Fig. 18. (a) Variation of SCG slope about a fixed point ($K_{Ia} = 7.18 \times 10^5 \, \text{N/m}^{1.5}$ and $v_c = 1.12 \times 10^{-6} \, \text{m/s}$) controlled by
657   parameters κ_0 and Q_0: $\kappa_0 = 0.60 \, \text{m}^{2.5}/\text{mol}$ and $Q_0 = 257720 \, \text{J/mol}$ for Simulation A; $\kappa_0 = 0.24 \, \text{m}^{2.5}/\text{mol}$ and
658 $Q_0 = 131000 \, \text{J/mol}$ for Simulation B; and $\kappa_0 = 0.10 \, \text{m}^{2.5}/\text{mol}$ and $Q_0 = 88760 \, \text{J/mol}$ for Simulation C. (b) Zoomed-in
659   presentation of Fig. 17 giving an impression of reduced stage-I slope.

660 This implies that a rate-limiting mechanism that is activated over a wide range of crack velocities can

661 cause the reduced slope in stage I. Perhaps a mechanism with weaker dependence on v_c compared to the

662 current transport models (e.g., a different near-tip diffusion mechanism, or sorption kinetics) can

663 potentially close this gap. In partial support of this hypothesis, the experimental SCG data for crack

664 propagation in liquid water in Fig. 16 which extends to much lower crack propagation velocities shows a

665 slope close to the in-vacuum one. This speculation challenges the commonly accepted picture that SCG

666 in stage I is free from any rate-limiting influences. More investigations are required in this regard to

667 clarify the origin of environment-dependent slope in stage I SCG.

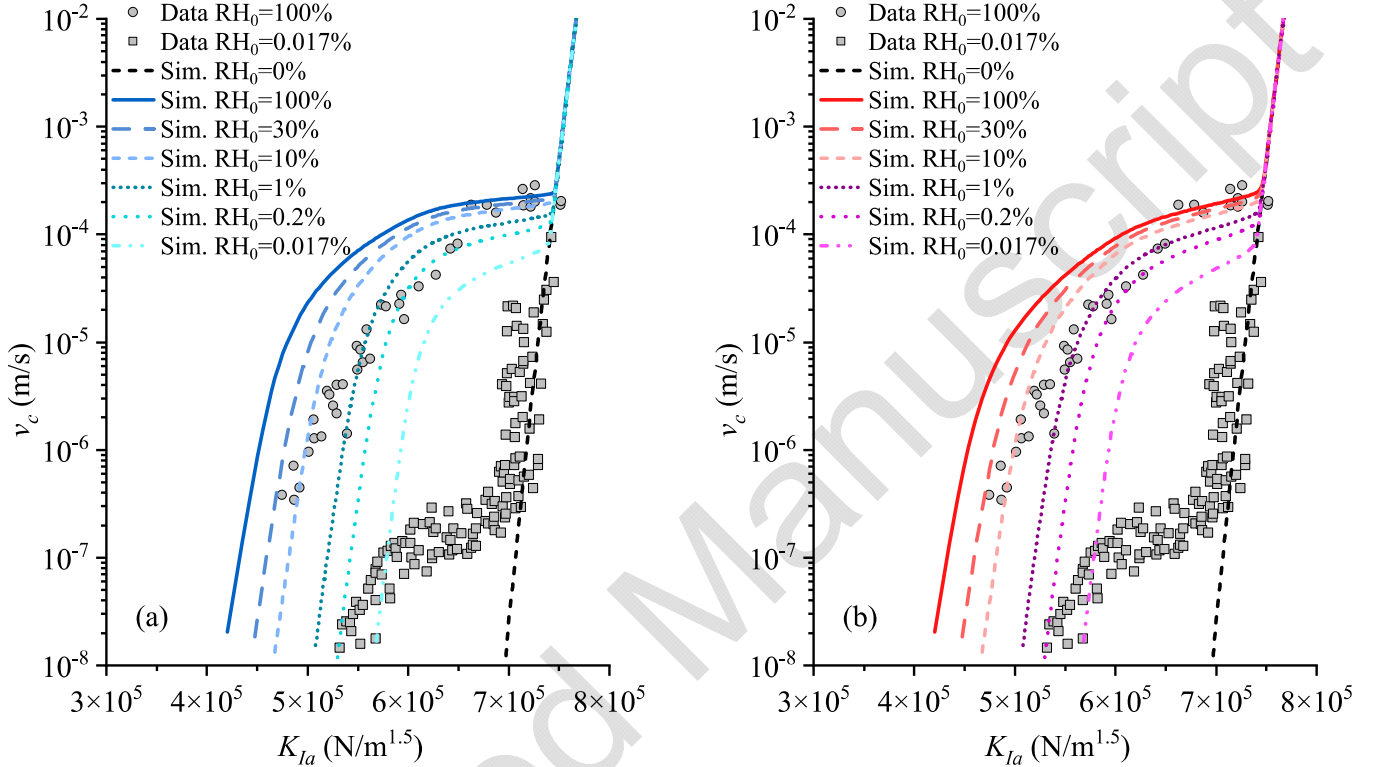668   Fig. 19 presents the predicted SCG curves over a range of relative humidity from 0% to 100%.

669
670 Fig. 19. Measured vs. predicted SCG curves at different RH_0 values based on (a) single regime flow and (b) dual regime flow
671 models.

672 It is observed that both flow models significantly underestimate the variation of plateau velocities at

673 different humidity levels. Based on our previous observation that the shape of SCG critically depends on

674 the transport model, we suspect that this underprediction is related to the insensitivity of the vapor

675 pressure profile $p(x)$ to the RH_0. Physically, the threshold crack width w_{th} characterizing the point of

676 transition from bulk flow to molecular diffusion (point C in Fig. 9c) should not be a constant but rather

677 vary with respect to the boundary conditions (i.e., the ambient humidity). This possibility is explored in

678 the next subsection.

679

680 **7.3. Effect of variable** w_{th}

681   Intuitively, lower RH means less water molecules in the environment, and they can be more easily

682   captured by the crack walls to form the first few adsorbed layers. This promotes the molecular diffusion

683   of water in adsorbed states rather than free bulk gas flow, thus extending the length of the "boundary

684   layer" d in Fig. 9a. w_{th} is therefore proposed to be inverse proportional to RH_0. A simple proposition

685   to account for this effect is:

686
$$w_{th} = \frac{\lambda / \mathrm{Kn}_0}{1 + h_0(\mathrm{RH}_0 - 1)} \tag{35}$$

687   where $h_0 < 1$ is a parameter to control how rapid w_{th} varies with RH_0 such that $w_{th}(\mathrm{RH}_0 = 1) = \lambda / \mathrm{Kn}_0$.

688   Here, a value of $h_0 = 0.919$ is found to match the plateau velocity for case of $\mathrm{RH}_0 = 0.017\%$. The

689   predicted SCG curves using the updated w_{th}, Eq. (35), for all other RH_0 values are presented in Fig. 20.

690   We can see that the SFFT model is now capable of quantitatively capturing the shifting of the plateau

691   velocity and the apparent fracture toughness under humidity changes. Again, this observation highlights

692   the importance of detailing the transport of sorptive species in the near-tip regime in order to correctly

693   predict the SCG behavior of brittle solids under various ambient conditions.

694   A subcritical cracking "stage diagram" can be produced (Fig. 21) in the normalized

695    $\log(v_c / v_0) - (K_{Ia} / \sqrt{2E'\gamma})$ space based on the slope of the predicted SCG curves in Fig. 20. The slope

696   in the normalized space is defined as $I_c = d\log(v_c / v_0) / d(K_{Ia} / \sqrt{2E'\gamma})$, which is analogous to the

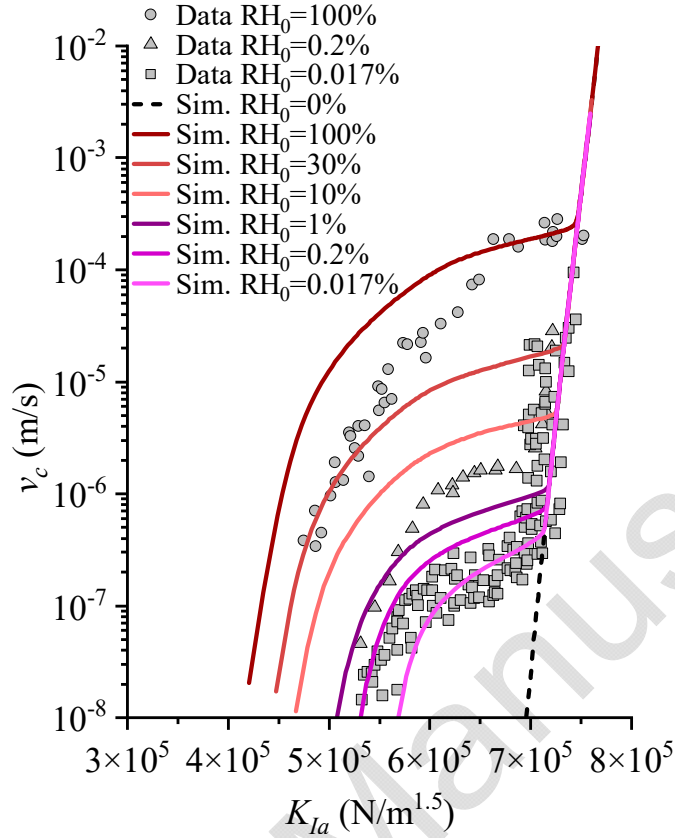697   *corrosion index* in the Charles' law (Atkinson, 1982).

Fig. 20. Measured vs. predicted SCG curves at different RH_0 values based on dual-regime flow and RH_0-dependent w_{th} (Eq. (35) with $h_0 = 0.919$).

701   It is apparent in Fig. 21 that stages I and III are represented by regions with larger I_c, while a drop of I_c

702   to lower values indicates stage II. Transition from stage II to III occurs abruptly (cyan dash-dot line),

703   while the transition from stage I to II happens gradually with a much smoother and wider variation of I_c

704   values in between. A value of $I_c = 15$ is selected to roughly represent this transition (pink dashed line).

705   Fig. 21 predicts that increased ambient relative humidity expands the stage-II zone, indicating that

706   species transport becomes more dominating in shaping the SCG curve over a wider K_{Ia} range at high

707   RH levels. If an SCG curve is plotted in a limited range of K_{Ia} and thus v_c, one would have concluded

708   that the apparent corrosion index (i.e., the slope) is reduced as a function of the ambient humidity. This

709   reiterates one of our earlier speculations that the reduced slopes in stage I SCG could be just a visual

710   impression of an extended stage II zone due to the slow transport of environmental agents.
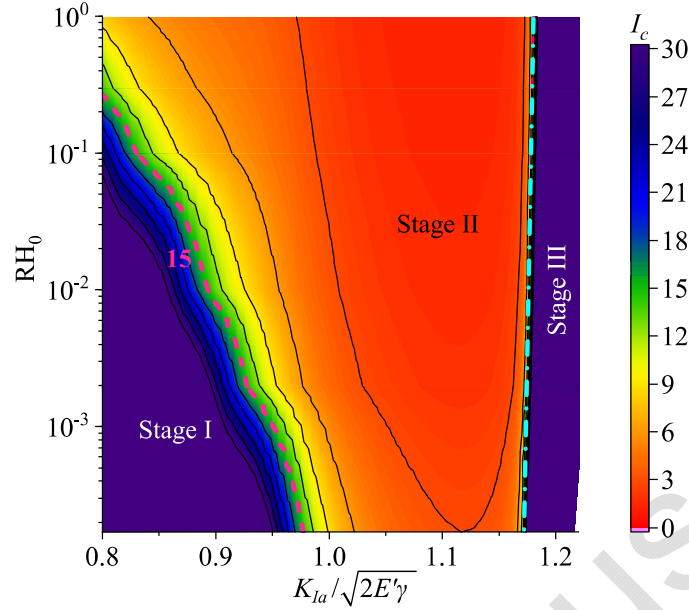
Fig. 21. A dimensionless stage diagram for SCG. Color indicates the slopes of normalized v_c / v_0 versus $K_{Ia} / \sqrt{2E'\gamma}$ curves from Fig. 20, based on which the three SCG stages can be clearly identified.

8. CONCLUSION

This study develops a surface-force based fracture theory (SFFT) to rationalize and predict the subcritical cracking of brittle solids in sorptive environments. The theory highlights the fundamental role of surface forces which present at a few tens of nanometer surface-surface separations on the apparent fracture toughness, its environmental dependency, and the crack growth kinetics of SCG. Specifically, analytical LEFM solutions are adopted to consider the repulsive disjoining force induced by sorption behind the crack tip. The competition between the material's intrinsic cohesive forces and environment-induced disjoining forces is manifested as the *effective stress intensity factor* operating at the crack tip and serves as the driving force for crack propagation. This quantitatively explains the environmentally induced strength reduction of brittle solids. The characteristic shape of the SCG curve is further impacted by the rate-limiting effect of species transport in the crack. Simplified analytical transport models are proposed to qualitatively represent the single-regime and dual-regime flows. Finally, the model is validated against the experimental data on soda-lime glass in water vapor studied by Wiederhorn (1967). The main findings of this study are highlighted below:

728   1. The development of repulsive disjoining pressure behind the crack tip in sorptive environment

729   can cause the reduction of apparent fracture toughness.

730   2. Species transport along the crack is the rate-controlling mechanism governing the plateau

731   velocity and the stage-II behavior of SCG.

732   3. The effect of transport can go beyond stage II and shape the characteristics of stage-I SCG curve,

733   for example, by reducing the apparent slope in stage I.

734   4. The SCG stage diagram generated by SFFT simulations allows one to visualize the conditions

735   for each stage of SCG and the characteristics of transition between stages.

736   The theory and its numerical solution scheme are set up in such a way that more complex and

737 advanced model components can be readily incorporated for extensions to other brittle materials. Further

738 improvements can be contemplated by (1) incorporating more realistic fluid transport models that

739 automatically capture the smooth transition between different transport mechanisms as the crack

740 aperture varies; (2) considering the underlying sources of surface forces to motivate a physics-based

741 disjoining pressure model; and (3) extending to different systems such as the SCG of quartz or calcite in

742 aqueous solutions for geoscience and geo-engineering applications. Some fundamental aspects require

743 further investigations to enrich the calibration and validation of SFFT. For example, experimental

744 studies and molecular dynamic simulations are needed to quantify disjoining pressure between freshly

745 exposed solid surfaces in sorptive environment and to better understand species transport in nano-

746 confined spaces.

747 **ACKNOWLEDGEMENT**

753   REFERENCES

754   572-1, D.E., 2012. Glass in Building–Basic Soda Lime Silicate Glass Products–Part 1: Definitions and
755   General Physical and Mechanical Properties. Beuth Verlag Berlin.
756   Acuña, S.M., Toledo, P.G., 2008. Short-range forces between glass surfaces in aqueous solutions.
757   Langmuir 24, 4881-4887.
758   Adapa, S., Malani, A., 2021. Role of cation size on swelling pressure and free energy of mica pores.
759   Journal of Colloid and Interface Science 599, 694-705.
760   Adler, J.J., Rabinovich, Y.I., Moudgil, B.M., 2001. Origins of the non-DLVO force between glass
761   surfaces in aqueous solution. Journal of colloid and interface science 237, 249-258.
762   Allegri, G., 2020. A unified formulation for fatigue crack onset and growth via cohesive zone modelling.
763   Journal of the Mechanics and Physics of Solids 138, 103900.
764   Ash, S.G., Everett, D.H., Radke, C., 1973. Thermodynamics of the effects of adsorption on interparticle
765   forces. Journal of the Chemical Society, Faraday Transactions 2 69, 1256.
766   Atkinson, B.K., 1982. Subcritical crack propagation in rocks: theory, experimental results and
767   applications. Journal of Structural Geology 4, 41-56.
768   Atkinson, B.K., 1984. Subcritical crack growth in geological materials. Journal of Geophysical Research:
769   Solid Earth 89, 4077-4114.
770   Barenblatt, G.I., 1962. The mathematical theory of equilibrium cracks in brittle fracture. Advances in
771   applied mechanics 7, 55-129.
772   Bažant, Z.P., Oh, B.H., 1983. Crack band theory for fracture of concrete. Matériaux et construction 16,
773   155-177.
774   Bazant, Z.P., Planas, J., 1997. Fracture and size effect in concrete and other quasibrittle materials. CRC
775   press.
776   Bird, R.B., Stewart, W.E., Lightfoot, E.N., 2006. Transport phenomena. John Wiley & Sons.
777   Brantut, N., Heap, M., Meredith, P., Baud, P., 2013. Time-dependent cracking and brittle creep in
778   crustal rocks: A review. Journal of Structural Geology 52, 17-43.
779   Brunauer, S., Deming, L.S., Deming, W.E., Teller, E., 1940. On a Theory of the van der Waals
780   Adsorption of Gases. Journal of the American Chemical Society 62, 1723–1732.
781   Chapman, S., Cowling, T.G., 1990. The mathematical theory of non-uniform gases: an account of the
782   kinetic theory of viscosity, thermal conduction and diffusion in gases. Cambridge university
783   press.
784   Charles, R., 1958. Static fatigue of glass. I. Journal of Applied Physics 29, 1549-1553.
785   Charles, R., 1962. The kinetics of glass failure by stress corrosion. Simposium sur la Resistance
786   Mechanique du Verre et les Moyens de l'Ameliorer 511.
787   Chester, F., Chester, J., Kronenberg, A., Hajash, A., 2007. Subcritical creep compaction of quartz sand
788   at diagenetic conditions: Effects of water and grain size. Journal of Geophysical Research: Solid
789   Earth 112.
790   Choi, J.-G., Do, D., Do, H., 2001. Surface diffusion of adsorbed molecules in porous media: Monolayer,
791   multilayer, and capillary condensation regimes. Industrial & engineering chemistry research 40,
792   4005-4031.

793 Cihan, A., Tokunaga, T.K., Birkholzer, J.T., 2019. Adsorption and capillary condensation-induced
794   imbibition in nanoporous media. Langmuir 35, 9611-9621.
795 Cihan, A., Tokunaga, T.K., Birkholzer, J.T., 2021. Diffusion‐to‐Imbibition Transition in Water
796   Sorption in Nanoporous Media: Theoretical studies. Water Resources Research,
797   e2021WR029720.
798 Clarke, D., Lawn, B., Roach, D., 1986. The role of surface forces in fracture, Fracture Mechanics of
799   Ceramics. Springer, pp. 341-350.
800 Crichton, S.N., Tomozawa, M., Hayden, J.S., Suratwala, T.I., Campbell, J.H., 1999. Subcritical crack
801   growth in a phosphate laser glass. Journal of the American Ceramic Society 82, 3097-3104.
802 Diao, Y., Espinosa-Marzal, R.M., 2016. Molecular insight into the nanoconfined calcite–solution
803   interface. Proceedings of the National Academy of Sciences 113, 12047-12052.
804 Dziadkowiec, J., 2019. Interactions between Confined Calcite Surfaces in Aqueous Solutions: A surface
805   forces apparatus study.
806 Dziadkowiec, J., Javadi, S., Bratvold, J.E., Nilsen, O., Røyne, A., 2018. Surface Forces Apparatus
807   measurements of interactions between rough and reactive calcite surfaces. Langmuir 34, 7248-
808   7263.
809 Dziadkowiec, J., Zareeipolgardani, B., Dysthe, D.K., Røyne, A., 2019. Nucleation in confinement
810   generates long-range repulsion between rough calcite surfaces. Scientific reports 9, 1-15.
811 Eppes, M., Hancock, G., Chen, X., Arey, J., Dewers, T., Huettenmoser, J., Kiessling, S., Moser, F.,
812   Tannu, N., Weiserbs, B., 2018. Rates of subcritical cracking and long-term rock erosion.
813   Geology 46, 951-954.
814 Eppes, M.C., Keanini, R., 2017. Mechanical weathering and rock erosion by climate‐dependent
815   subcritical cracking. Reviews of Geophysics 55, 470-508.
816 Eskandari-Ghadi, M., Zhang, Y., 2021. Mechanics of shrinkage-swelling transition of microporous
817   materials at the initial stage of adsorption. International Journal of Solids and Structures 222,
818   111041.
819 Eskandari-Ghadi, M., Zhang, Y., 2022. Modeling sorption-induced deformation of porous media: effect
820   of pore size distribution. International Journal of Solids and Structures (Under Review).
821 Freiman, S.W., Wiederhorn, S.M., Mecholsky, J., John J, 2009. Environmentally enhanced fracture of
822   glass: a historical perspective. Journal of the American Ceramic Society 92, 1371-1382.
823 Gdoutos, E.E., 2020. Fracture mechanics: an introduction. Springer Nature.
824 Hillerborg, A., Modéer, M., Petersson, P.-E., 1976. Analysis of crack formation and crack growth in
825   concrete by means of fracture mechanics and finite elements. Cement and concrete research 6,
826   773-781.
827 Irwin, G.R., 1957. Analysis of stresses and strains near the end of a crack traversing a plate.
828 Israelachvili, J.N., 2011. Intermolecular and surface forces. Academic press.
829 Jennings, S., 1988. The mean free path in air. Journal of Aerosol Science 19, 159-166.
830 Karimpour, H., Lade, P.V., 2010. Time effects relate to crushing in sand. Journal of Geotechnical and
831   Geoenvironmental Engineering 136, 1209-1219.
832 Kilburn, C.R., Voight, B., 1998. Slow rock fracture as eruption precursor at Soufriere Hills volcano,
833   Montserrat. Geophysical Research Letters 25, 3665-3668.
834 Kim, J., Aluru, N., Tortorelli, D., 2003. Improved multi‐level Newton solvers for fully coupled multi‐
835   physics problems. International journal for numerical methods in engineering 58, 463-480.
836 Lawn, B., 1974. Diffusion-controlled subcritical crack growth in the presence of a dilute gas
837   environment. Materials Science and Engineering 13, 277-283.

838 Lawn, B.R., 1975. An atomistic model of kinetic crack growth in brittle solids. Journal of Materials
839   Science 10, 469-480.
840 Lawn, B.R., 1985. Interfacial forces and the fundamental nature of brittle cracks. Applied physics letters
841   47, 809-811.
842 Le, J.-L., Bažant, Z.P., Bazant, M.Z., 2009. Subcritical crack growth law and its consequences for
843   lifetime statistics and size effect of quasibrittle structures. Journal of Physics D: Applied Physics
844   42, 214008.
845 Lennartz-Sassinek, S., Main, I., Zaiser, M., Graham, C., 2014. Acceleration and localization of
846   subcritical crack growth in a natural composite material. Physical Review E 90, 052401.
847 Li, D., Wei, D., 2020. Rate-Dependent Cohesive Zone Model for Fracture Simulation of Soda-Lime
848   Glass Plate. Materials 13, 749.
849 MAI, Y.W., Lawn, B.R., 1987. Crack‐interface grain bridging as a fracture resistance mechanism in
850   ceramics: II, Theoretical fracture mechanics model. Journal of the American Ceramic Society 70,
851   289-294.
852 Meng, F., Thouless, M., 2019. Cohesive-zone analyses with stochastic effects, illustrated by an example
853   of kinetic crack growth. Journal of the Mechanics and Physics of Solids 132, 103686.
854 Meyland, M.J., Nielsen, J.H., Kocer, C., 2021. Tensile behaviour of soda-lime-silica glass and the
855   significance of load duration–A literature review. Journal of Building Engineering, 102966.
856 Michalske, T.A., Freiman, S.W., 1982. A molecular interpretation of stress corrosion in silica. Nature
857   295, 511-512.
858 Nara, Y., Morimoto, K., Hiroyoshi, N., Yoneda, T., Kaneko, K., Benson, P.M., 2012. Influence of
859   relative humidity on fracture toughness of rock: implications for subcritical crack growth.
860   International Journal of Solids and Structures 49, 2471-2481.
861 Needleman, A., 1990. An analysis of tensile decohesion along an interface. Journal of the Mechanics
862   and Physics of Solids 38, 289-324.
863 Nguyen, O., Repetto, E., Ortiz, M., Radovitzky, R., 2001. A cohesive model of fatigue crack growth.
864   International Journal of Fracture 110, 351-369.
865 Olson, J.E., 1993. Joint pattern development: Effects of subcritical crack growth and mechanical crack
866   interaction. Journal of Geophysical Research: Solid Earth 98, 12251-12265.
867 Planas, J., Elices, M., 1991. Nonlinear fracture of cohesive materials, Current trends in concrete fracture
868   research. Springer, pp. 139-157.
869 Rice, J.R., 1978. Thermodynamics of the quasi-static growth of Griffith cracks. Journal of the
870   Mechanics and Physics of Solids 26, 61–78.
871 Røyne, A., Dalby, K.N., Hassenkam, T., 2015. Repulsive hydration forces between calcite surfaces and
872   their effect on the brittle strength of calcite‐bearing rocks. Geophysical Research Letters 42,
873   4786-4794.
874 Sills, R., Thouless, M., 2015. Cohesive-length scales for damage and toughening mechanisms.
875   International Journal of Solids and Structures 55, 32-43.
876 Simmons, G.W., Pao, P., Wei, R., 1978. Fracture mechanics and surface chemistry studies of subcritical
877   crack growth in AISI 4340 steel. Metallurgical Transactions A 9, 1147-1158.
878 Tada, H., 1972. Studies of the crack opening stretch concept in application to several fracture problems.
879   Lehigh University.
880 Tada, H., Paris, P., Irwin, G., 2000. The analysis of cracks handbook. New York: ASME Press 2, 1.
881 Tijssens, M., Van der Giessen, E., Sluys, L., 2000. Modeling of crazing using a cohesive surface
882   methodology. Mechanics of Materials 32, 19-35.

883 Tsilingiris, P., 2008. Thermophysical and transport properties of humid air at temperature range between
884   0 and 100 C. Energy Conversion and Management 49, 1098-1110.
885 Tvergaard, V., Hutchinson, J.W., 1992. The relation between crack growth resistance and fracture
886   process parameters in elastic-plastic solids. Journal of the Mechanics and Physics of Solids 40,
887   1377-1397.
888 Wan, K.-T., Aimard, N., Lathabai, S., Horn, R.G., Lawn, B.R., 1990. Interfacial energy states of
889   moisture-exposed cracks in mica. Journal of Materials Research 5, 172-182.
890 Wiederhorn, S., 1967. Influence of water vapor on crack propagation in soda-lime glass. Journal of the
891   American Ceramic Society 50, 407-414.
892 Wiederhorn, S., 1969. Fracture surface energy of glass. Journal of the American Ceramic Society 52,
893   99-105.
894 Wiederhorn, S., 1974. Subcritical crack growth in ceramics, Fracture mechanics of ceramics. Springer,
895   pp. 613-646.
896 Wiederhorn, S., Bolz, L., 1970. Stress corrosion and static fatigue of glass. Journal of the American
897   ceramic society 53, 543-548.
898 Wiederhorn, S., Fuller Jr, E., Thomson, R., 1980. Micromechanisms of crack growth in ceramics and
899   glasses in corrosive environments.
900 Wiederhorn, S.M., Fuller Jr, E.R., 1989. Effect of surface forces on subcritical crack growth in glass.
901   Journal of the American Ceramic Society 72, 248-251.
902 Wu, K., Li, X., Wang, C., Yu, W., Chen, Z., 2015. Model for surface diffusion of adsorbed gas in
903   nanopores of shale gas reservoirs. Industrial & Engineering Chemistry Research 54, 3225-3236.
904 Xu, X., Xu, J., Chen, J., Li, P., Liu, B., Li, Y., 2017. Investigation of dynamic multi-cracking behavior
905   in PVB laminated glass plates. International Journal of Impact Engineering 100, 62-74.
906 Yaminsky, V., Stewart, A., 2003. Interaction of glass surfaces in air: Dispersion forces in the retarded
907   regime. Langmuir 19, 4037-4039.
908 Zhang, Y., Buscarnera, G., 2018. Breakage mechanics for granular materials in surface-reactive
909   environments. Journal of the Mechanics and Physics of Solids 112, 89-108.

910

911 **APPENDIX A.   NUMERICAL SOLUTION TO THE Π-w SYSTEM**

912   The solution to the $\Pi - w$ system involves finding a consistent set of $\Pi(x)$ and $w(x)$ that satisfy

913   two equations of the general forms $w(x) = w(x, \Pi(x))$ and $\Pi(x) = \Pi(x, w(x))$. Eq. (2) is an example of

914   the former, and Eqns. (9) and (10) take the form of the latter.

915   To write Eq. (2) in discrete form, an approximation for the integral on the right-hand side is required.

916   Such approximation is commonly performed by adopting Gauss quadrature methods. However, due to

917   the singularity of the fundamental solution, Eq. (4),   at $x = s$, Gauss quadrature approximation

918   encountered numerical convergence issues. Here an alternative approximation is adopted. Refer to the

919   spatial discretization in Section 6. First, the disjoining pressure over the range of x_i and x_{i+1}, $\Pi_i^{elem}(x)$,

920   is approximated with a constant value, $\Pi_i^{elem} = (\Pi(x_i) + \Pi(x_{i+1}))/2 = (\Pi_i + \Pi_{i+1})/2$. With this, Eqns. (1)

921   and (2) can be written at each node as

922
$$w(x_i) = c_\sigma(x_i)\sigma + \sum_{j=1}^{N-1} \Pi_j^{elem} \underbrace{\int_{s=s_j}^{s=s_{j+1}} c_\Pi(x_i, s)ds}_{\mathbf{c}_\Pi^{elem}} \text{ and } K_{Ie} = k_{I\sigma}\sigma + \sum_{j=1}^{N-1} \Pi_j^{elem} \underbrace{\int_{s=s_j}^{s=s_{j+1}} k_{I\Pi}(s)ds}_{\mathbf{k}_{I\Pi}^{elem}} \qquad (A.1)$$

923   The fundamental functions $c_\Pi(x,s)$ and $k_{I\Pi}(s)$ are now the crack opening profile and the stress

924   intensity factor for uniformly distributed stress over range (s_j, s_{j+1}) in Fig. A.1a, which are non-singular.

925   For unit repulsive stress ($\Pi = 1$) applied over length s in Fig. A.1b, Tada (1972) provides

926
$$\int_0^s c_\Pi(x,s)ds = \frac{8(1-v^2)}{\pi E} \left\{ \begin{array}{l} \sqrt{a^2 - x^2} \sin^{-1}\frac{s}{a} + \frac{1}{2}|x-s|\cosh^{-1}\frac{a^2 - sx}{a|x-s|} \\ +\frac{1}{2}|x+s|\cosh^{-1}\frac{a^2 + sx}{a|x+s|} \end{array} \right\} \qquad (A.2)$$

927
$$\int_0^s k_{I\Pi}(s)ds = 2\sqrt{\frac{a}{\pi}}\sin^{-1}\frac{s}{a} \qquad (A.3)$$
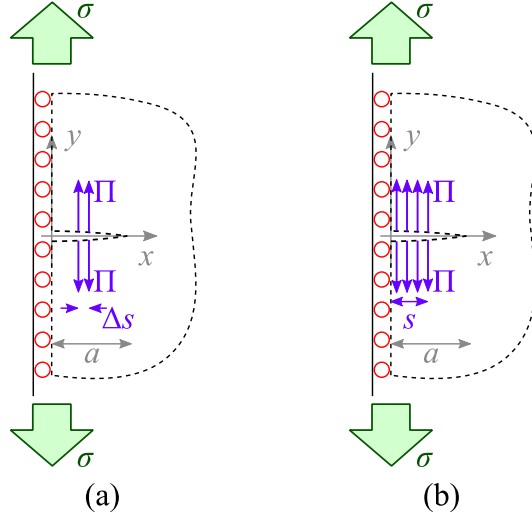
928
929   Fig. A.1 Geometry considered in (a) this paper in deriving the fundamental solutions and (b) Tada (1972).

930   The fundamental solutions for uniform stress over an arbitrary segment (s_j, s_{j+1}) in the integrals of

931   Eq. (A.1) can be directly expressed in terms of Eqns. (A.2) and (A.3), as

932    $\int_{s=s_j}^{s=s_{j+1}} c_{\Pi}(x_i, s)ds = \int_0^{s_{j+1}} c_{\Pi}(x_i, s)ds - \int_0^{s_j} c_{\Pi}(x_i, s)ds$ and $\int_{s=s_j}^{s=s_{j+1}} k_{I\Pi}(s)ds = \int_0^{s_{j+1}} k_{I\Pi}(s)ds - \int_0^{s_j} k_{I\Pi}(s)ds$.

933    $c_{\sigma}(x_i)$ and $k_{I\sigma}$ are given by Eq. (3). Eq. (A.1) can be written in a fully discretized form

934    $$w_i = c_{\sigma,i}\sigma + \sum_{j=1}^{N-1} c_{\Pi,ij}^{elem}\Pi_j^{elem} \text{ and } K_{Ie} = k_{I\sigma}\sigma + \sum_{j=1}^{N-1} k_{I\Pi,j}^{elem}\Pi_j^{elem} \tag{A.4}$$

935   where $c_{\sigma,i} = c_{\sigma}(x_i)$. $\Pi_i^{elem} = (\Pi_i + \Pi_{i+1})/2$ can also be written as a tensor transformation, $\mathbf{\Pi}^{elem} = \mathbf{A}_{\Pi} \cdot \mathbf{\Pi}$,

936   where

937    $$\mathbf{A}_{\Pi} = \begin{bmatrix} \frac{1}{2} & \frac{1}{2} & 0 & 0 & & 0 & 0 \\ 0 & \frac{1}{2} & \frac{1}{2} & 0 & \cdots & 0 & 0 \\ 0 & 0 & \frac{1}{2} & \frac{1}{2} & & 0 & 0 \\ & \vdots & & & \ddots & 0 & 0 \\ 0 & 0 & 0 & 0 & 0 & \frac{1}{2} & \frac{1}{2} \end{bmatrix}_{(N-1)\times N} \tag{A.5}$$

938   Finally, Eq. (A.4) can be written in matrix-vector notation as:

939    $$\mathbf{w} = \mathbf{c}_{\sigma}\sigma + \mathbf{c}_{\Pi} \cdot \mathbf{\Pi} \tag{A.6}$$

$$K_{Ie} = k_{I\sigma}\sigma + \mathbf{k}_{I\Pi} \cdot \mathbf{\Pi} \tag{A.7}$$

940

941 where $\mathbf{c}_\Pi = \mathbf{c}_\Pi^{elem} \cdot \mathbf{A}_\Pi$ and $\mathbf{k}_{I\Pi} = \left(\mathbf{k}_{I\Pi}^{elem}\right)^T \cdot \mathbf{A}_\Pi$. Substituting the relation $\Pi = \Pi(w, p)$ into Eq. (A.6)

942 yields a nonlinear algebraic equation that can be solved iteratively. The solution is sought here by

943 rewriting Eq. (A.6) in the same way as Planas and Elices (1991):

$$\mathbf{\Pi}(\mathbf{w}, \mathbf{p}) - \mathbf{M} \cdot \mathbf{w} + \mathbf{L}\sigma = \mathbf{0} \tag{A.8}$$

944

945 where $\mathbf{p}$ is the nodal vector of gas partial pressure assumed to be known and constant in this local solver,

946 $\mathbf{M} = \mathbf{c}_\Pi^{-1}$, and $\mathbf{L} = \mathbf{c}_\Pi^{-1} \cdot \mathbf{c}_\sigma$. A Newton-Raphson iteration method is implemented to seek the solution w_i

947 at each node. Starting with an initial guess, $\mathbf{w}_0$, the correction $\mathbf{w}_{k+1} = \mathbf{w}_k + \delta\mathbf{w}_k$ at iteration k is made

948 where $\delta\mathbf{w}_k = -(\mathbf{J}^M)^{-1} \cdot \mathbf{R}^M$. $\mathbf{R}^M$ and $\mathbf{J}^M$ are computed as

$$R_i^M = \Pi(w_i, p_i) - M_{ij}w_j + L_i\sigma \text{ and } J_{ij}^M = \left.\frac{\partial \Pi}{\partial w}\right|_{w_i, p_i} \delta_{ij} - M_{ij} \tag{A.9}$$

949

950 with $\mathbf{w} = \mathbf{w}_k$. The search for solution continues until the error defined as

$$\varepsilon_M = \sqrt{\sum_1^{N-1} (R_i^M)^2 \Delta x_i} \tag{A.10}$$

951

952 is reduced below a tolerance (here taken as 5×10^{-4}). Once Π and w profiles are obtained, Eq. (A.7)

953 computes K_{Ie} to conclude the $\Pi - w$ system solver.

954   Our $\Pi - w$ system solver is verified by comparing the computed crack opening profile with the

955 analytical crack opening solutions of Tada et al. (2000) subjected to different surface force distributions
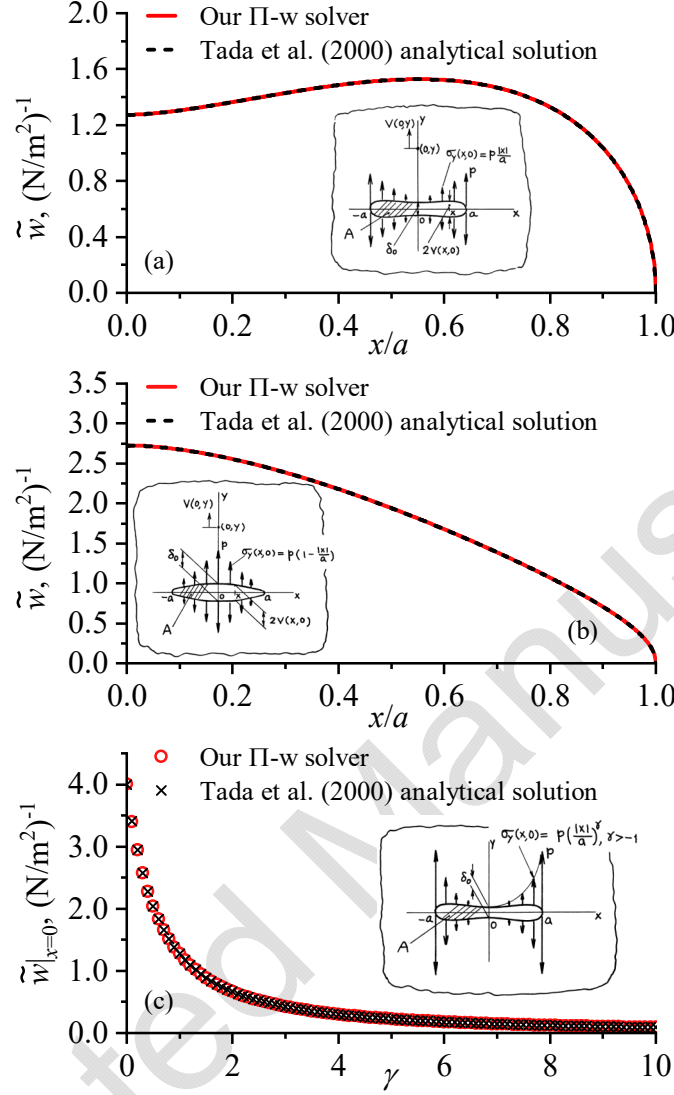
956 (Fig. A.2).

957

Fig. A.2 Verification of the normalized crack opening profile, $\tilde{w} = wE / (1 - v^2)a$, with exact solutions (Tada et al., 2000) for surface force distributions (a) linearly increasing toward the crack tip; (b) linearly decreasing toward the crack tip; and (c) nonlinearly increasing toward the crack tip. Figure insets are courtesy of Tada et al. (2000).

APPENDIX B.   INITIAL GUESS FOR $T > 0$ AND $T = 0$

The current implementation is stress-controlled (i.e., σ and a vary between timesteps). The crack velocity is small and the timesteps are close, thus the variation of a over timesteps is very small. However, a small variation in σ can create a large change in K_{Ie} which exponentially updates v_c and

966   subsequently $p(x)$. It is thus apparent that using the solution at timestep t_k as the initial guess for

967   timestep t_{k+1} can involve large errors and prevent convergence.

968   We can obtain an initial guess for timestep t_{k+1} by a linear extrapolation. The rate of change of the

969   solution vector, $\mathbf{u}$, over time Δt is linearized based on a small variation of σ over a small time $. \theta\Delta t .$ as

970
$$\frac{\Delta \mathbf{u}}{\Delta t} \approx \frac{\mathbf{u}\,|_{\sigma(t_k + \theta\Delta t)} - \mathbf{u}\,|_{\sigma(t_k)}}{\theta\Delta t} \tag{B.1}$$

971   The value of θ is set to 10^{-2}. Since the variation of σ over the time interval $\theta\Delta t$ is now small, the

972   solution at time t_k works as a good initial guess for the solution at time $t_k + \theta\Delta t$. Thus, $\mathbf{u}\,|_{\sigma(t_k + \theta\Delta t)}$ is

973   found using the same partitioned Newton-Raphson solver with the initial guess of $\mathbf{u}\,|_{\sigma(t_k)}$. The sole

974   purpose of $\mathbf{u}\,|_{\sigma(t_k + \theta\Delta t)}$ is to assist with finding a reasonable initial guess for $\mathbf{u}\,|_{\sigma(t_k + \Delta t)}$, it can thus be

975   calculated with a more relaxed tolerance to reduce simulation time. Then, the initial guess for time t_{k+1}

976   is computed via linear extrapolation:

977
$$\mathbf{u}\,|_{\sigma(t_k + \Delta t)} \approx \mathbf{u}\,|_{\sigma(t_k)} + \frac{\Delta \mathbf{u}}{\Delta t}\Delta t \tag{B.2}$$

978   While the procedure described here involves an additional set of iterations in search of $\mathbf{u}\,|_{\sigma(t_k + \theta\Delta t)}$, the

979   amount of computation required for those iterations is far less than that required for finding the solution

980   to $\mathbf{u}\,|_{\sigma(t_k + \Delta t)}$ using the initial guess $\mathbf{u}\,|_{\sigma(t_k)}$ even if the latter converges.

981   The initial guess for $t = 0$ can be obtained by starting simulations with a small σ so that v_c can be

982   predicted a few orders of magnitude smaller than $d\,/\,D$. This way, the fluid profile is known, $p(x) = p_0$.

983   Thus, the $\Pi - w$ system can be solved alone for K_{Ie}. One must then verify that this K_{Ie} results in v_c of

984   similar magnitude as the predicted one.